CHALMERS
UNIVERSITY OF TECHNOLOGY

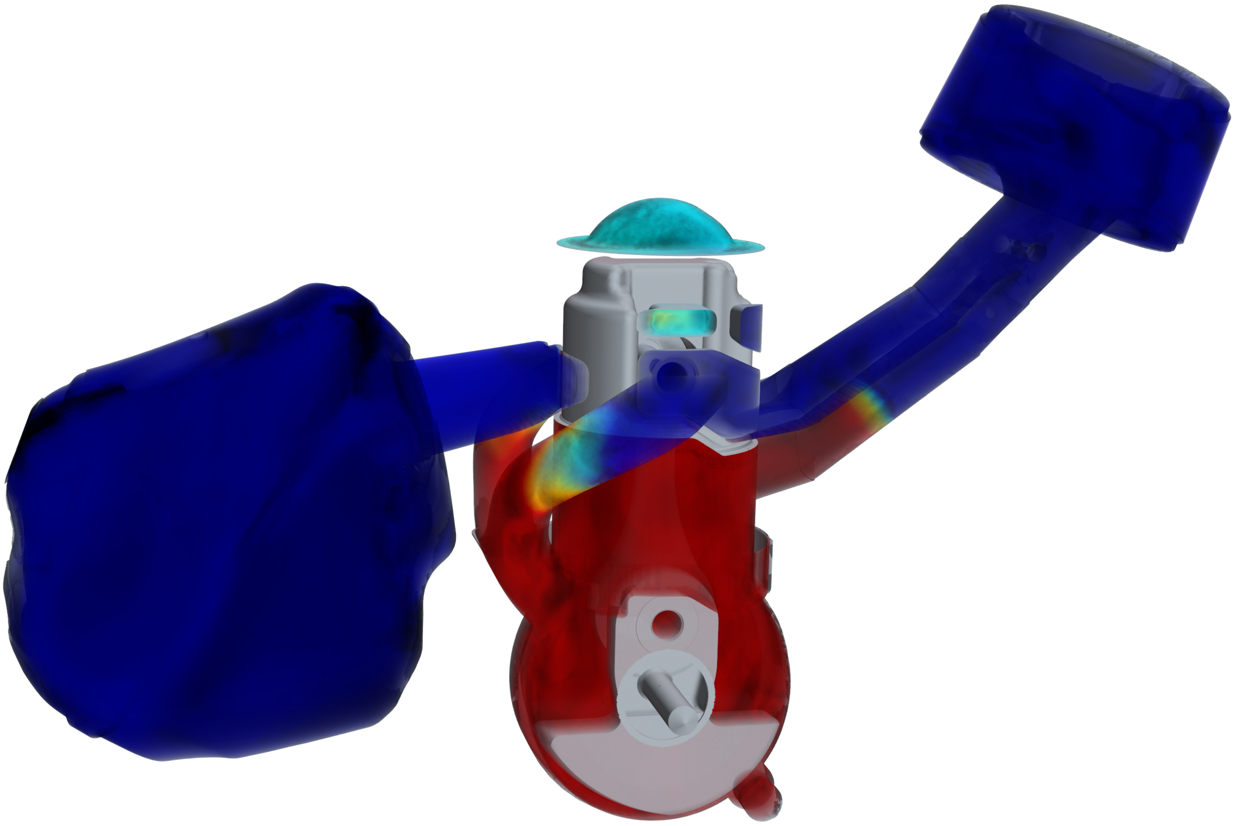

Development of a Simplified CFD Model for In-Cylinder Flow in Two-Stroke Engines

Master's thesis in Applied Mechanics

Emil Andersson
Tyra Dernfalk

DEPARTMENT OF MECHANICS AND MARITIME SCIENCES
CHALMERS UNIVERSITY OF TECHNOLOGY
Gothenburg, Sweden 2026
www.chalmers.se

Master's Thesis in Applied Mechanics

Development of a Simplified CFD Model for In-Cylinder Flow in Two-Stroke Engines

Emil Andersson
Tyra Dernfalk

Department of Mechanics and Maritime Sciences
Division of Fluid Dynamics
Chalmers University of Technology
Gothenburg, Sweden 2026

Development of a Simplified CFD Model for In-Cylinder Flow in Two-Stroke Engines

Emil Andersson
Tyra Dernfalk

Supervisor: Simon Hjalmarsson, Husqvarna AB
Examiner: Niklas Andersson, Mechanics and Maritime Sciences

Master's Thesis 2026
Department of Mechanics and Maritime Sciences
Chalmers University of Technology
SE-412 96 Gothenburg
Sweden
Telephone +46 31 772 1000

Cover: An illustration of the CFD model of the two stroke engine in StarCCM+, showing the mass fraction of fresh fuel from its minimum in blue to its maximum in red.

Typeset in LaTeX
Gothenburg, Sweden 2026

Development of a Simplified CFD Model for In-Cylinder Flow in Two-Stroke Engines
Emil Andersson
Tyra Dernfalk
Department of Mechanics and Maritime Sciences
Division of Fluid Dynamics
Chalmers University of Technology

Abstract

With ever stricter emission laws, a main focus in the development of new chainsaws is not only to optimize the performance but also to lessen the environmental impact from the operation of the two-stroke engine. A big part of this is to optimize the geometry to reduce the leakage of unburned fuel. Long simulation times makes this process slow and tedious. This thesis investigates different ways of reducing the simulation time to enable a faster design iteration process in the future. This is done by removing non-vital geometry to reduce the size and complexity of the domain. The mesh is also examined to assess which areas can be coarsened and thereby reduce the number of cells. Furthermore the physics setup and time discretization of the simulation is studied. These are modified by increasing the time step and changing a gas model. Finally, the successful changes from the three different approaches are combined into one single model. To verify that the changes made does not impact the results of the simulations significantly, several measurements are set up in the model with extra focus towards quantities like the pressures that later can be measured easily in a physical prototype. The study results in a simplified model which runs more than three times faster compared to the original, without significantly reducing the accuracy of the results.

Keywords: CFD, Two-stroke engine, Wiebe, Stratified charge, Overset mesh, Chainsaw, Adaptive time step

Preface

This report presents the outcome of our master's thesis project carried out at the Department of Mechanics and Maritime Sciences at Chalmers University of Technology in collaboration with Husqvarna during the spring of 2026.

Acknowledgements

We want to express our gratitude to the people at Husqvarna for the opportunity to write our thesis together with them. In particular we want to devote a big thank you to our supervisor Simon Hjalmarsson who has supported us in our work and helped review the report, and to our overseeing manager Jonas Haglind. Furthermore, we would like to thank Frans Levin who we could rely on to always be at the office if we had any questions, as well as the rest of the people at the Advanced CAE department for creating a friendly and enjoyable working environment. We would also like to thank our examiner Niklas Andersson and opponent Alrik Sjökvist for their helpful feedback.

Emil Andersson, Tyra Dernfalk, Gothenburg, June 2026

List of Acronyms

Below is the list of acronyms that have been used throughout this thesis listed in alphabetical order:

Af	Air-fuel
AFR	Air-fuel Ratio
Ah	Airhead
APE	Absolute Percentage Error
BDC	Bottom Dead Center
CAD	Crank Angle Degree
CC	Combustion Chamber
CFD	Computational Fluid Dynamics
CFL	Courant Friedrich and Lewy condition
DNS	Direct Numerical Simulations
DR	Delivery Ratio
EOC	End of Combustion
HRR	Heat Release Rate
LES	Large Eddie Simulations
LPFI	Low Pressure Fuel Injection
MAE	Mean Absolute Error
MFB	Mass Fraction Burned
NMAE	Normalized Mean Absolute Error
RANS	Reynolds-Averaged Navier–Stokes
SOC	Start of Combustion
SV	Swept Volume
TDC	Top Dead Center
TE	Trapping Efficiency

Nomenclature

Below is the nomenclature of indices, sets, parameters, and variables that have been used throughout this thesis.

Indices

i, j, k	Dummy index
l	Gas species index
t	Time

Parameters

m	Combustion mode parameter
x_b	Burned fuel fraction
λ	Ratio of air to fuel ratios in combustion chamber at SOC

Variables

A_t	Actual value
C	Convective Courant number
C_p, C_v	Specific heat
C_μ	Turbulence model constant
D	Molecular diffusivity
Dk_{eff}	Effective diffusivity of k
$D\varepsilon_{eff}$	Effective diffusivity of epsilon
d	Distance to wall
F_t	Measured data
f	Body force

G_k	Generation of turbulent kinetic energy
h	Enthalpy
i	internal energy
K	Thermal conductivity
k	Turbulent kinetic energy
M_{as}	Fresh charge mass into the CC
M_{dr}	Reference air mass required to fill the CC
M_{tas}	Trapped mass from current cycle
m_{air}	Mass of air
m_{fuel}	Mass of fuel
N	Number of data points
n	Number of gas components
p	Pressure
Q	Heat release
Q_{wall}	Heat transfer to walls
R_u	Universal gas constant
Re_D	Wall-distance Reynolds number
S_i	Energy source term
S_{ij}	Strain-rate tensor
S_M	Mass source term
Sc	Schmidt number
s	Stroke
T	Temperature
t	Time
u, v	Velocity
u^*	Velocity scale
V	Volume
X	Species mole fraction
x, y	Position
Y	Species mass fraction
y^+	Wall Y-plus
γ	Specific heat ratio
γ_t	Blending coefficient
Δt	Time step size

Δx	Grid spacing
$\Delta\theta$	Combustion duration
δ_{ij}	Kronecker delta
ε	Dissipation
θ	Crank angle
θ_{SOC}	Crank angle at start of combustion
μ	Dynamic viscosity
ν	Kinematic viscosity
ν_t	Turbulent viscosity
ρ	Density
Φ	Viscous dissipation
ϕ	Fluid property
ϕ_{mix}	Mixture property
$\bar{\Omega}_{ij}$	Mean rate of rotation tensor
ω	Angular velocity

Contents

List of Figures

List of Tables

1

Introduction

This chapter describes the background of the thesis and outlines the limitations and goal.

1.1 Background

Husqvarna AB is a company that manufactures a wide range of products, mainly for gardening and construction. Even if many of the products are becoming electric, some of them still need to be driven using combustion engines to handle long operating hours in places where recharging opportunities are limited. Therefore some of their chainsaws, like the one in Fig. 1.1, are utilizing two-stroke engines. Two stroke engines are known to have high emissions but there is a strong focus on minimizing these.

Figure 1.1: Husqvarna chainsaw 564 XP [1]. Reprinted with permission.

One of the general problems with two-stroke engines is that they tend to leak unburned fuel out of the combustion chamber, causing higher emissions [2]. This leakage can be minimized by altering the design.

To get results without physical testing in the developing stages, a computational fluid dynamics (CFD) model can be used to simulate the flow inside the engine.

Complex CFD models need a lot of computational power, which is often a problem when trying to improve existing designs. The main contributors to the complexity of the model are, among others, a fine mesh and a complex geometry. When reducing these, the key is to preserve the most important data from the simulation. The purpose of these specific simulations is to retrieve the pressures inside the engine and also properties of the outflow. The CFD model currently used in the design process is very time consuming when used for design iterations, which is why the task is to simplify it to allow for a faster and more automated optimization process.

1.2 Purpose and Goal

The purpose of this master's thesis is to develop a simplified CFD model in Star-CCM+ which reduces the computational time, making it better suited for working with design iterations. The flow should remain accurate, and the combustion chamber is of high interest. The pressures inside the two-stroke engine has to be captured correctly as well. The goal is to reduce the computational time by at least 50% compared to the current model without a major difference in the results.

1.3 Limitations

The complete model is set up in Siemens Simcenter Star-CCM+ 2502, hence this is the software that will be used. The thesis will only investigate one specific two-stroke engine model at its rated speed. This is due to chainsaws being used in a wide range of speeds, making it unfeasible to run simulations for all operating points.

The model will remain three-dimensional, 2D simulations will not be investigated. The results are evaluated based on reference data extracted from the original simulation, not from experimental data. The changes will still be set up with the experimental process in mind to make it possible to compare data extracted from experiments.

The combustion model used today is already one of the simplest and cheapest models [3] and due to this, the thesis will not look into other options for the combustion process.

There are a couple ways of handling movement in StarCCM+ in regards to the mesh, this thesis uses the overset mesh approach.

2

Theory

This chapter will outline relevant theory related to the thesis.

2.1 The Two-Stroke Engine

An illustration of a two stroke engine with part numbering is presented in Fig. 2.1.

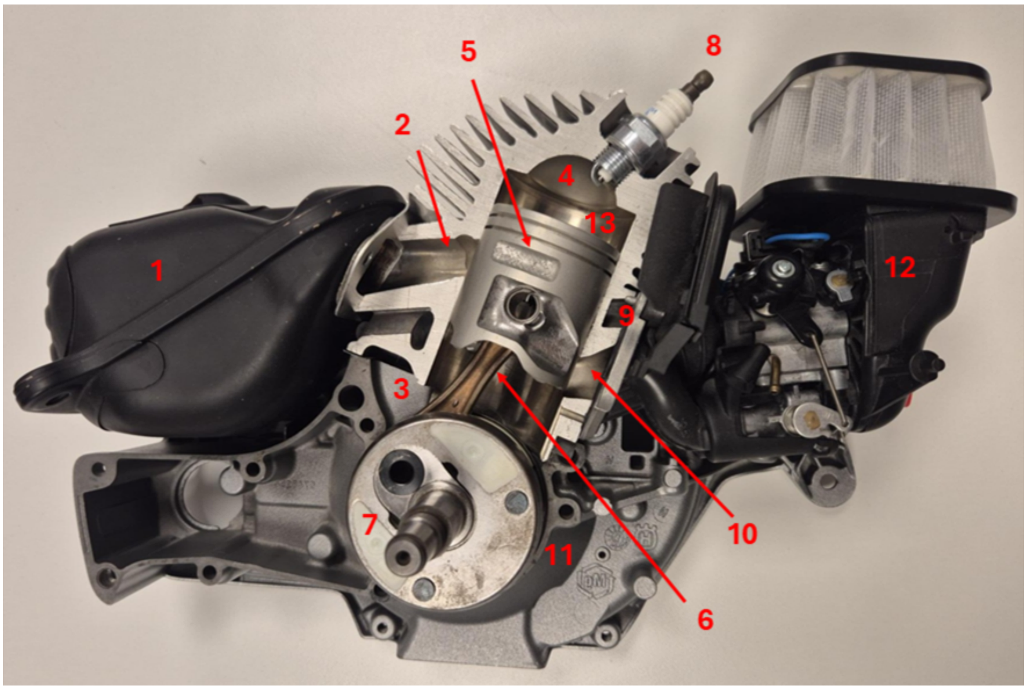

Figure 2.1: Cross-section of a two-stoke engine.

On the right side of the engine, air is drawn in through the inlet system (12). The incoming air is split into two channels, one where fuel will be injected either through a carburetor or via low pressure fuel injection (LPFI), and one with clean air. An inlet port is located at (10), from which a mixture of air and fuel (Af) flows into the crankcase (11). Above the Af-port, two airhead (Ah) ports are placed (9). This is where clean air can flow into the scavenging channel (3) through cutouts in the piston (5). The scavenging channel connects the crankcase to the cylinder (13), allowing for the gas mixture to flow into the combustion chamber (CC) (4) through the scavenging ports, where the spark plug (8) ignites the gases. The exhaust channel (2) is located to the left of the piston, this is where the exhaust gases escapes into the muffler (1) after the combustion process has taken place. In the middle of the figure, the connecting rod (6) can be seen connecting the piston to the crank (7).

A complete cycle of the engine consists of two strokes. When the piston moves upward, referred to as the compression stroke, the gas in the combustion chamber gets compressed by the moving piston [4]. As the piston rises, the scavenging channel is closed off, and no more gas can enter the combustion chamber. The exhaust port is open a little bit longer, before it too is closed off by the piston. The piston continues upward until it reaches its top dead center (TDC). While this is happening, the inlet ports are opened and new gas can begin to flow into the crankcase.

As the combustion takes place, the piston starts to move downwards again, referred to as the expansion stroke [4]. The exhaust port is once again opened to let the exhaust gases out of the combustion chamber. As it moves further down towards its bottom dead center (BDC), the scavenging port is opened to let fresh charge into the combustion chamber, and the inlet ports are closed off.

2.1.1 Airhead

Airhead, or as it is more commonly known, sequential stratified charge, is a technique implemented in the two-stroke engine to reduce emissions of unburned fuel [5] [6]. As can be seen in Fig. 2.2, while the piston is close to TDC, clean air can flow into the scavenging channel via cavities inside the piston. The clean air can be seen in blue, flowing from right to left.

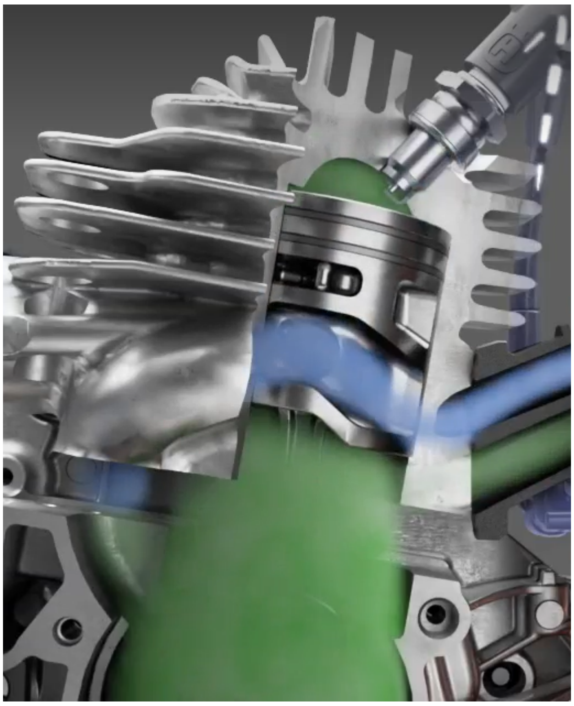

Figure 2.2: Flow of air (in blue) through the Ah-port and the piston into the scavenging channel [1]. Reprinted with permission.

With this technique, a layering of the gases is created inside the scavenging channel, with clean air on top of the Af-mixture [5]. Utilizing this, if there is any leakage out of the exhaust port when the gases flow through the combustion chamber, the first thing to escape is the clean air. Thereby giving the exhaust port more time to close completely, trapping the Af-mixture inside the chamber.

2.1.2 Engine Performance Parameters

To measure the performance of an engine there are several parameters that can be used, such as the trapping efficiency (TE), the delivery ratio (DR), and λ.

If there is exactly enough oxygen present in the mixture to burn all of the fuel, the combustion process would be called stoichiometric [7]. A ratio of the real air to fuel ratio (AFR) and the stoichiometric AFR is used as a measurement and is referred to as λ, (see Eq. 2.1).

$$\lambda = \frac{AFR}{AFR_{stoich}} \tag{2.1}$$

The AFR in the combustion chamber is defined as [7]:

$$AFR = \frac{m_{air}}{m_{fuel}} \tag{2.2}$$

If the combustion takes place with more oxygen than required, $\lambda > 1$, the burning process is called lean [8]. And if there is less oxygen than required, $\lambda < 1$, the burning process is called rich.

The delivery ratio is defined below as [9]:

$$DR = \frac{M_{as}}{M_{dr}} \tag{2.3}$$

Here M_{as} is the mass of the air flowing into the crankcase and M_{dr} is the theoretical air mass needed to fill the entire swept volume (SV) [9]. The SV is defined by Eq. 2.4, where the bore is the diameter of the piston, and s denotes the stroke length [10].

$$SV = \left(\frac{bore}{2}\right)^2 \pi s \tag{2.4}$$

The trapping efficiency is defined as [9]

$$TE = \frac{M_{tas}}{M_{as}} \tag{2.5}$$

where M_{tas} represents the trapped mass from the current cycle.

2.2 Wiebe

The Wiebe combustion model is a one-equation model that describes the combustion process. The mass fraction burned (MFB), x_b, can be calculated using Eq. 2.6, where θ is the current crank angle, θ_{SOC} is the crank angle at the start of combustion (SOC), and $\Delta\theta$ is the combustion duration [3],[11].

$$x_b(\theta) = 1 - exp\left[-a\left(\frac{\theta - \theta_{SOC}}{\Delta\theta}\right)^{m+1}\right] \tag{2.6}$$

The parameter a is a constant defined by Eq. 2.7, where $x_{b,EOC}$ is the burned fuel fraction at the end of combustion (EOC).

$$a = -ln(1 - x_{b,EOC}) \tag{2.7}$$

To retrieve the unknown parameter, m, the Wiebe function is fitted against experimental data for the MFB [12]. One way to obtain the MFB is to integrate the heat release rate (HRR), which corresponds to the MFB [13]. To compute the HRR Eq. 2.8 can be used.

$$HRR = \frac{dQ}{d\theta} = \frac{\gamma}{\gamma - 1}p\frac{dV}{d\theta} + \frac{1}{\gamma - 1}V\frac{dp}{d\theta} + \frac{dQ_{wall}}{d\theta} \tag{2.8}$$

The fitting can be done in different ways, but is usually done using a least square method [14].

2.3 Computational Fluid Dynamics

CFD is a technique in which the governing equations, (see Chpt. 2.3.1), are numerically solved [15], [16]. The equations are usually solved using one of three main approaches, these being the finite element, finite difference, and finite volume methods. The domain in which the equations are to be solved is discretized into a grid known as a mesh, and the equations are then solved for each of these grid cells in the form of systems of linear equations. When using CFD for engine simulations, time steps are often of the order of 0.25 crank angle degrees (CAD) [17] or smaller [18].

2.3.1 Governing Equations

The governing equations for a compressible Newtonian fluid are the conservation of mass, conservation of energy, and conservation of momentum [19].

The conservation of mass, commonly referred to as the continuity equation, is defined by Eq. 2.9.

$$\frac{\partial p}{\partial t} + div(\rho\mathbf{u}) = 0 \tag{2.9}$$

The conservation of energy equation can be found in Eq. 2.10.

$$\frac{\partial(\rho i)}{\partial t} + div(\rho i \mathbf{u}) = -p\, div\, \mathbf{u} + div(K\, grad\, T) + \Phi + S_i \tag{2.10}$$

For a perfect gas:

$$p = \rho RT, i = C_v T \tag{2.11}$$

Where C_v is the specific heat at a constant volume [20]. The conservation of linear momentum is presented component wise in Eq. 2.12-2.14 [19].

$$\frac{\partial(\rho u)}{\partial t} + div(\rho u \boldsymbol{u}) = -\frac{\partial p}{\partial x} + div(\mu\, grad\, u) + S_{Mx} \tag{2.12}$$

$$\frac{\partial(\rho v)}{\partial t} + div(\rho v \boldsymbol{u}) = -\frac{\partial p}{\partial y} + div(\mu\, grad\, v) + S_{My} \tag{2.13}$$

$$\frac{\partial(\rho w)}{\partial t} + div(\rho w \boldsymbol{u}) = -\frac{\partial p}{\partial z} + div(\mu\, grad\, w) + S_{Mz} \tag{2.14}$$

To use the equations, they are discretized over finite control volumes, called cells, in CFD simulations.

2.3.2 Turbulence Model

There are several ways to resolve turbulence in the flow, large eddie simulations (LES), direct numerical simulations (DNS), or by solving the Reynolds-Averaged Navier–Stokes (RANS) equations [21]. The Navier Stokes equations are presented in Eq. 2.15 [22].

$$\begin{cases} \frac{\partial \rho}{\partial t} + \rho \frac{\partial v_i}{\partial x_i} = 0 \\ \rho \frac{dv_i}{dt} = -\frac{\partial P}{\partial x_i} + \frac{\partial}{\partial x_i}\left(2\mu S_{ij} - \frac{2}{3}\mu \frac{\partial v_k}{\partial x_k}\delta_{ij}\right) + \rho f_i \end{cases} \tag{2.15}$$

When working with turbulent flows, the Navier–Stokes equation is often time averaged first to obtain the RANS equations [22]. When doing so, new unknowns called Reynolds stresses appears which then need to be modeled. One of the models developed for this is the k-ε model. This approach is less computationally expensive than both LES and DNS [23]. It consists of two equations, one solving for the turbulent kinetic energy (k) and one for the turbulence eddy dissipation (ε) [24]. The standard k-ε model uses the equations presented in Eq. 2.16 and Eq. 2.17 to determine the turbulent viscosity (ν_t) defined in Eq. 2.18 [24] .

$$\frac{\partial k}{\partial t} + \frac{\partial k u_i}{\partial x_i} = \frac{\partial}{\partial x_i}\left(Dk_{eff}\frac{\partial k}{\partial x_i}\right) + G_k - \varepsilon \tag{2.16}$$

$$\frac{\partial \varepsilon}{\partial t} + \frac{\partial \varepsilon u_i}{\partial x_i} = \frac{\partial}{\partial x_i}\left(D\varepsilon_{eff}\frac{\partial \varepsilon}{\partial x_i}\right) + C_{1\varepsilon}\frac{\varepsilon}{k}G_k - C_{2\varepsilon}\frac{\varepsilon^2}{k} \tag{2.17}$$

$$\nu_t = C_\mu \frac{k^2}{\varepsilon} \tag{2.18}$$

G_k is the production of turbulent kinetic energy as a result of mean velocity gradients, determined by [24]:

$$G_k = 2\nu_t S_{ij}^2 \tag{2.19}$$

The strain rate tensor is given as:

$$S_{ij} = 0.5\left(\frac{\partial u_j}{\partial x_i} + \frac{\partial u_i}{\partial x_j}\right) \tag{2.20}$$

Dk_{eff} and $D\varepsilon_{eff}$ are the effective diffusivities and can be calculated using the equations below:

$$Dk_{eff} = \nu + \nu_t \tag{2.21}$$

$$D\varepsilon_{eff} = \nu + \frac{\nu_t}{\sigma_\varepsilon} \tag{2.22}$$

σ_ε is usually set equal to 1.3, $C_{1\varepsilon}$=1.44, $C_{2\varepsilon}$=1.92, and C_μ=0.09.

The realizable k-ε model introduces another equation for ε, and also changes the formulation of the eddy viscosity model by changing the constant C_μ, to a varying function that enables usage for large strain rates [25]. The new equation for ε is presented in Eq. 2.23 [24].

$$\frac{\partial \varepsilon}{\partial t} + \frac{\partial \varepsilon u_i}{\partial x_i} = \frac{\partial}{\partial x_i}\left(D\varepsilon_{eff}\frac{\partial \varepsilon}{\partial x_i}\right) + \sqrt{2}C_{1\varepsilon}S_{ij}\varepsilon - C_{2\varepsilon}\frac{\varepsilon^2}{k+\sqrt{v\varepsilon}} \tag{2.23}$$

The turbulent viscosity is defined as in the standard k-ε but uses the varying C_μ defined by Eq. 2.24 instead of the constant value.

$$C_\mu = \frac{1}{A_0 + A_s\frac{kU^*}{\varepsilon}} \tag{2.24}$$

U^* can be written as:

$$U^* = \sqrt{S_{ij}S_{ij} + \tilde{\Omega}_{ij}\tilde{\Omega}_{ij}} \tag{2.25}$$

With:

$$\tilde{\Omega}_{ij} = \overline{\Omega}_{ij} - \varepsilon_{ijk}\omega_k - 2\varepsilon_{ijk}\omega_k \tag{2.26}$$

A_0 is set to 4 and $A_s = \sqrt{6}cos\varphi$ with:

$$\varphi = \frac{1}{3}Arccos(min(max(\sqrt{6}W, -1), 1)) \tag{2.27}$$

$$W = \frac{S_{ij}S_{jk}S_{ki}}{\tilde{S}^2} \tag{2.28}$$

$$C_{1\varepsilon} = max\left(\frac{\eta}{5+\eta}, 0.43\right) \tag{2.29}$$

Where:

$$\eta = S\left(\frac{k}{\varepsilon}\right) \tag{2.30}$$

The constants are set as $C_2 = 1.9$, $\sigma_k = 1.0$, and $\sigma_\varepsilon = 1.2$

The realizable k-ε two-layer model is a combination of the two-layer approach and the realizable k-ε model [26]. This gives the model flexibility for all y^+ wall treatment. The two layer approach allows for the use of the k-ε model in the entire flow affected by the wall. The difference is that the values of the dissipation rate and the turbulent viscosity are changed depending on the distance to the wall. Close to the wall they are a function of the turbulent length scale, further out in the flow they are instead interpolated with the freestream values.

The equations are derived for incompressible flow. In the compressible solver in Star-CCM+ the equations are adjusted to take the compressibility into consideration [26].

2.3.3 Mesh

A mesh is a partition of the computational domain into a fine grid of cells and the governing equations are then solved iteratively for each cell [15]. There are two main types of meshes, structured and unstructured, with the unstructured meshes being better at capturing arbitrary geometries.

In Star-CCM+, there are three main types of volume meshes, these being tetrahedral, trimmed cell, and polyhedral meshes, visualized in Fig. 2.3-2.5 [26]. The tetrahedral mesher builds the mesh by inserting points into the domain with the Delaunay method. The trimmed cell mesher utilizes a pure hexahedral grid that covers the geometry, and the cells at the edges of the domain are then trimmed using the surfaces of the geometry. Finally the polyhedral mesh is built from a tetrahedral mesh. It consists of cells of arbitrary shapes with an average of 14 faces per polyhedral.

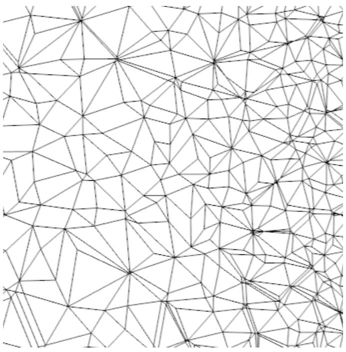

Figure 2.3: Tetrahedral mesh.

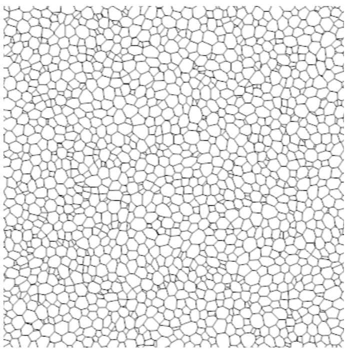

Figure 2.4: Polyhedral mesh.

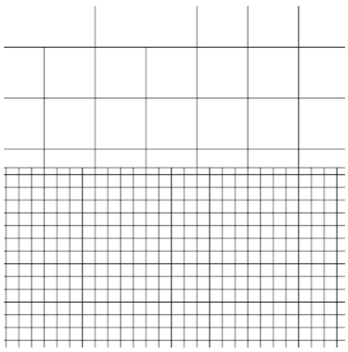

Figure 2.5: Trimmed cell mesh.

One way of evaluating the level of resolution of the mesh, is by utilizing the parameter y^+ and the Courant number.

2.3.3.1 Prism Layers

Prism layers are used to refine the near-wall regions in the domain. This is done to better capture the boundary layer regions [26]. The prism mesh consists of orthogonal prismatic cells along boundary surfaces .

2.3.3.2 Wall Y^+

The Wall y^+ is a normalized measure of the distance to the wall and the definition is presented in Eq. 2.31, where u^* is the friction velocity [26].

$$y^+ = \frac{y\rho u^*}{\mu} \tag{2.31}$$

For y^+ values below five, in the viscous sub layer [27], the velocity scale can be defined as seen below [26]:

$$u^* = \sqrt{\frac{\mu|\mathbf{v}_{tangential}|}{\rho y}} \tag{2.32}$$

Similarly the velocity scale for y^+ values above 30, in the log-layer [27], can be defined as below [26]:

$$u^* = C_\mu^{1/4} k^{1/2} \tag{2.33}$$

In the two-layer approach, the blended wall function is used for the friction velocity everywhere and it is defined as [26]:

$$u^* = \gamma_t \sqrt{\frac{\mu|\mathbf{v}_{tangential}|}{\rho y}} + (1-\gamma_t) C_\mu^{1/4} k^{1/2} \tag{2.34}$$

and the blending function, γ_t, as:

$$\gamma_t = exp\left(-\frac{Re_D}{11}\right) \tag{2.35}$$

With Re_D being the wall-distance Reynolds number defined by the equation below:

$$Re_D = \frac{\sqrt{k}d}{\nu} \tag{2.36}$$

The y^+ values should aim to be around 1 or above 30 when using a two layer approach for the k-ε model [26].

2.3.3.3 CFL

The convective Courant number describes how many cells the fluid moves per time step, see Eq. 2.37 [26]. When using an implicit solver, one should aim for an average Courant number of ≈ 1 to achieve stability.

$$C = \frac{v\Delta t}{\Delta x} \tag{2.37}$$

2.3.3.4 Overset Mesh

With the use of overset meshes, there are two or more meshes that are overlapping [28]. The cells in these meshes are divided into active and inactive cells. In one of the meshes, it is the so called acceptor cells that determine if they are active or not. In the cells that are inactive nothing is solved. The same goes for the other mesh/meshes where the so called donor cells determine whether the cells in that/those meshes is active or not.

Overset meshes are often used when there are moving parts in a simulation [29]. One region, usually the stationary, is being used as the background mesh while moving parts, together with a small volume around them, are meshed as overset meshes. In Star-CCM+, an interface is created for the overset mesh between two regions. Via a hole-cutting process, the meshes are divided into active and inactive cells, and which of the cells that will be the acceptor cells is determined. It is important that the cells in both regions are of similar size in the overlap region and that both meshes have at least five cells in the overlapping region.

When using the overset mesh approach, one needs to monitor the mass conservation in the simulations [30]. If all of the meshes resolves the flow correctly, the interpolation between them will conserve the mass, however, if one of them does not, the mass will not be conserved across the overset meshes.

2.3.4 Multi-component Gas

The multi-component gas module is a single fluid formulation that computes the fluid properties in a few different ways, depending on the property [26]. Some properties such as for example the specific heat are calculated according to Eq. 2.38 where Y_l is the mass fraction of component l, ϕ_l is the corresponding property and n is the total number of gas components.

$$\phi_{mix} = \sum_{l=1}^{n} Y_l \phi_l \tag{2.38}$$

The dynamic viscosity and thermal conductivity are calculated using the Mathur-Saxena averaging method defined in Eq. 2.39, where X_l is the species mole fraction of component l.

$$\phi = \frac{1}{2}\left(\sum_{l=1}^{n} X_l \phi_l + \left(\sum_{l=1}^{n} \frac{X_l}{\phi_l}\right)^{-1}\right) \tag{2.39}$$

To determine the molecular diffusivity of each component in the mixture, $D_{l,m}$, the Schmidt number is used as below:

$$Sc_l = \frac{\nu}{D_{l,m}} \tag{2.40}$$

2.3.5 Enthalpy

When working with perfect gases, the enthalpy only varies with the temperature as can be seen below [31]:

$$h(T_1) = h(T_0) \int_{T_0}^{T_1} C_p dT \tag{2.41}$$

To determine the enthalpy of a certain gas, the 7-coefficient NASA thermodynamic polynomials can be used [26]. The polynomial for the enthalpy is defined as below:

$$\frac{h}{R_u T} = a_1 + \frac{a_2}{2}T + \frac{a_3}{3}T^2 + \frac{a_4}{4}T^3 + \frac{a_5}{5}T^4 + \frac{a_6}{T} \tag{2.42}$$

The coefficients for each individual gas can be retrieved from a material database.

2.4 Error Measurements

The absolute percentage error (APE) [32] is quantified as in Eq. 2.43. Where A_t is the reference value and F_t the measured data.

$$APE = \left| \frac{A_t - F_t}{A_t} \right| \tag{2.43}$$

The mean absolute error (MAE) [33], is defined as in Eq: 2.44, where N stands for the number of measurements.

$$MAE = \frac{1}{N} \sum_{t=1}^{N} |A_t - F_t| \tag{2.44}$$

3

Current setup

The model is simulating the process of a Schnürle two-stroke engine with three moving parts; the piston, the connecting rod, and the crank. The combustion process is not simulated but modeled using the Wiebe model and the mesh is a polygonal mesh with prism layers along all surfaces.

3.1 Geometry

In Fig. 3.1 a cross-section of the simulation model is presented.

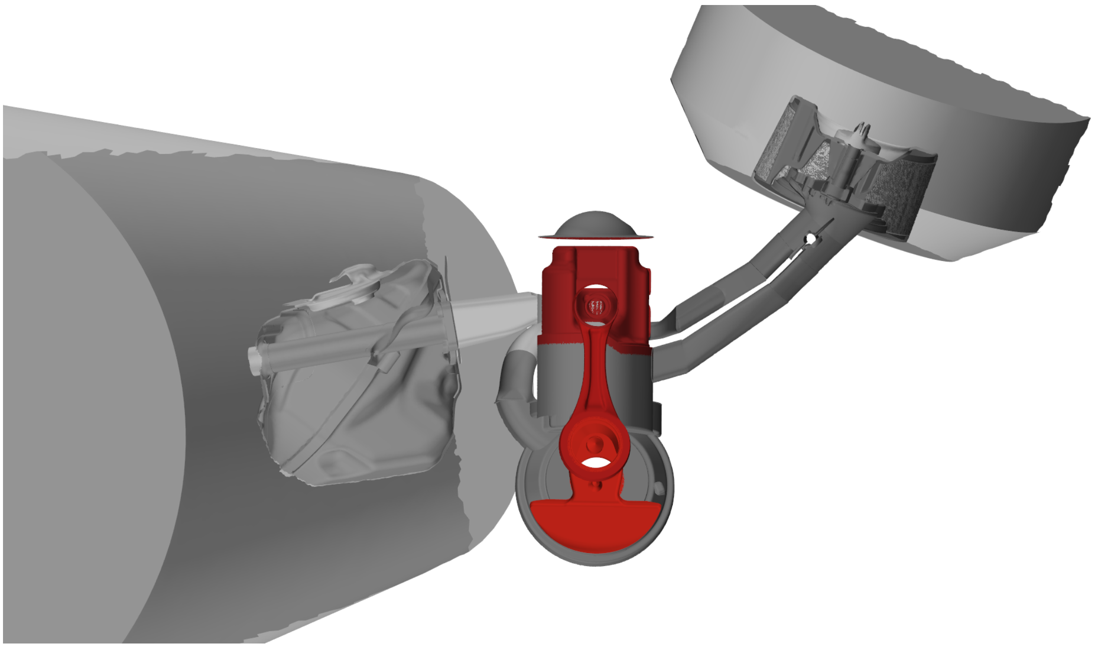

Figure 3.1: Illustration of the model in Star-CCM+ with the moving parts in red.

Furthest to the right, there is a cone around the intake filter, where atmospheric conditions are applied. The filter and the intake can be seen connecting to the crankcase at two different locations, the lower one being the Af-channel and the upper one being the Ah-channel. Even if the crankcase and cylinder are different parts, they are defined as one single region in the setup. The red part at the bottom of the crankcase is the crank and it is attached to the piston via the connecting rod.

At the upper left of the crankcase, the scavenging channels can be seen connecting to the cylinder. At the top, the combustion chamber is seen and to the left of the cylinder, in a lighter shade of gray, the exhaust is illustrated connecting to the muffler. The large cone around the muffler is, just as the one around the intake, set to atmospheric conditions.

3.2 Motion

There are three moving parts in the simulations; the piston, the connecting rod, and the crank, these can be seen marked red in Fig. 3.1. Each of the parts have separate movement definitions, that ensures that the movements are synced. The motion of the pistons is purely translational, and the crank motion is purely rotational. The motion of the connecting rod is a combination of both translation and rotation as it is connecting the piston and the crank.

3.3 Fuel Injection

The CFD model does not simulate the fuel injection as in the real chainsaw. Instead a portion at the end of the Af-pipe is defined as a cell set, illustrated in Fig. 3.2, and a source term adding fuel mass is then applied to the set. The source term is defined in a way that accounts for the mass flow, and the current gas composition in the section so that the mass fraction of fuel into the crankcase is constant.

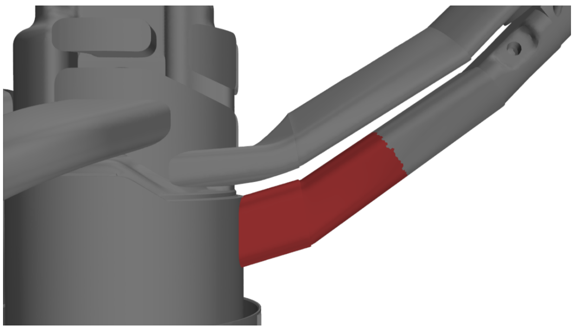

Figure 3.2: Cell set marked in red where the fuel is added as a source term.

3.4 Combustion Process

The combustion process is activated as the piston moves upward, and starts to approach its TDC. There is no spark plug to ignite the gases since the combustion is utilizing the Wiebe model which determines how much of the fuel is burned with repect to time. As the combustion occurs, source terms handles the exchange of molecules allowing for the oxygen and fuel to be reformed into carbon dioxide and water. This process continues until either the fuel or the oxygen runs out and the combustion no longer can proceed.

3.5 Mesh

Apart from the regular mesh, all moving parts have an overset mesh associated with them. This means that when the parts move there is no need to re-mesh the regions. Instead the overset meshes handles the information exchange. Since the overset meshes for all the moving regions overlap at some point, overset interfaces are created between them all. This is also done for all moving regions and the background mesh, which is the cylinder-crankcase since it is stationary, and since all movement are inside this mesh. All meshes, both overset and background, are utilizing prism layers and polygonal cells to capture the characteristics of the flow.

3.6 Numerical Setup

The current simulation setup is using a coupled unsteady implicit solver with a fixed time step of 0.25 CAD. The fluid is simulated as a multi-component gas, consisting of five different species: carbon dioxide, fuel, water, nitrogen, and oxygen. The turbulence is modeled using the realizable two-layer k-ε model.

4
Method

The existing model is first analyzed to understand how everything is set up and defined. Before any modifications are made, measurements are set up in the original model to be used as reference data later. The process is divided into three main areas where the first examines the possible geometrical modifications, the second the mesh and the third the physics of the model. The changes and simplifications are run just a few revolutions at first to determine if they look promising enough to keep, and to find if there are any issues that needs to be addressed before running them until convergence. One thing is changed at a time and the successful changes are later combined to establish an optimal model.

4.1 Preprocessing

The first step was to set up measurements in the existing model to collect data that can be used as reference values for the modified versions. Some scenes were also created to help visualize certain aspects of the flow such as the mass fraction of fuel and the pressure. A scene is a representation of the results or the setup that could be including the geometry or a field of the flow for example.

Some measurements were also set up to allow for the use of boundary conditions instead of the inlet and outlet geometries. For the inlet, the total temperature, total pressure, and mass fractions were measured at a plane just upstream of the Ah- and Af-ports. Inside the muffler, several pressure measurements were taken, a volume-averaged pressure for a sphere occupying almost the entire muffler, a surface-average over the exit of the muffler and a surface-average at the boundary between the muffler and the exhaust pipe.

Reports and plots were created to enable validation of the results from the simplified models. The performance parameters; DR, TE, and λ were calculated, and mass flows were measured over the Ah-, Af-, scavenging-, and exhaust-ports. This was not only done to compare the mass flows for the reference and the new models, but also to compute the mass conservation. The internal pressure in the crankcase and inside the combustion chamber are evaluated as mass averages.

4.2 Changes and Modifications

The modifications were divided into three major categories. The first one being geometrical modifications, where different parts were removed and replaced with either boundary conditions or stationary volumes. Another approach is mesh modifications, where the mesh was studied to see if and where it can be coarsened or changed in other ways to save computational time without compromising the accuracy of the results significantly. The last category was the physical setup where the changes were made to the gas mixture and the time stepping.

4.3 Geometrical Modifications

The geometrical changes were divided into several main categories, the outlet, the inlet and the moving parts inside the crankcase. Each of the changes were implemented individually at first to assess the impact, and some were later combined.

4.3.1 Simplified Outlet

To reduce the model size, the parts downstream of the exhaust pipe i.e the muffler and the big atmospheric cone, were removed. The first approach was to set the end of the exhaust pipe to a pressure outlet with the measured pressure. Later this was changed by using a small cone around the exhaust exit instead, similar to the one around the muffler. This was done to minimize the numerical issues caused by having the pressure outlet to close to the exhaust port. The cone boundaries could then be set to pressure outlets instead.

Multiple versions were set up using the different pressure measurement from the muffler to see which gave the best match. One version was also set up with atmospheric pressure to see if it was feasible to use this setup without requiring any prior data. As for the mass fraction at the boundary, it was set to the standard air values. This needs to be specified for the software to be able to handle any potential backflow over the outlet boundary, and what is specified should therefore not affect the simulation as a whole.

4.3.2 Simplified Inlet

A model was set up where the majority of the inlet-system were removed. Only the part of the pipes closest to the crankcase for the Ah- and Af-channels are left. The end of the pipes were set up as stagnation inlets, with the measured total temperatures and total pressures as the boundary conditions. By removing the majority of the inlet pipes, the air filter, and the atmosphere, and instead applying these stagnation inlets at the remaining pipe boundary, the need for the fuel injection also disappeared. Instead, since the gas mass fraction is known for both pipes, this can be specified directly at the boundary.

4.3.3 Limiting Moving Parts

Out of the three moving parts, the piston is the most essential for the function of the engine, but the possibility of removing the other two was investigated. By reducing the number of moving parts in the model, the number of overset meshes can be limited, speeding up the simulation.

4.3.3.1 Replaced Connecting Rod

One setup was made where the connecting rod was removed from the model. This was done by eliminating the connecting rod and replacing the corresponding volume with a cylinder that was merged with the crank instead. This allowed for the two volumes to move together as one. The volume of the connecting rod was measured by meshing the solid rod and then using a report to compute the total volume of the mesh. This volume was then created as a small cylinder directly in Star-CCM+, which was then merged with the crank using the unite tool. The new geometry is presented in Fig. 4.1.

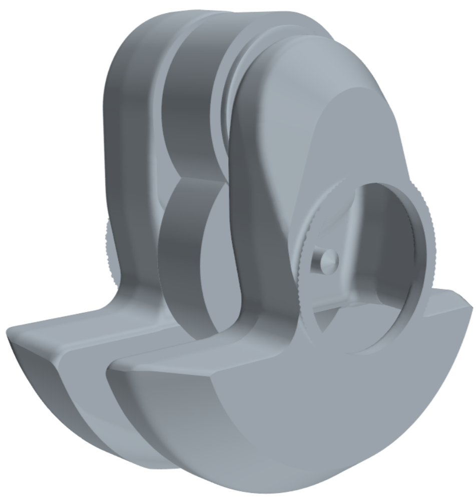

Figure 4.1: The crank with the volume of the connecting rod replaced.

To create the overset region, an offset was created based on the united part. The unite was then subtracted from the offset, meaning that the solid parts were not meshed since no fluid is present here. The subtracted volume was then meshed with the same settings as the original crank. To ensure that the air volume is kept constant in the crankcase, an overset volume integral was computed and compared for the new model and the reference model. When necessary, the added cylinder was modified until the air volumes matched.

4.3.3.2 Replaced Crank

One option is to keep the connecting rod but to take away the rotating crank. The volume of the crank was calculated in the same way as for when the connecting rod was removed, first meshing and measuring the volume using a summation report and then computing the air volume. To allow for the connecting rod to still move freely, two stationary cylinders were placed inside the crankcase with a spacing between them for the rod to pass through, and both cylinders were subtracted from the crankcase.

4.3.3.3 Replaced Connecting Rod and Crank

One step further is to remove both the crank and the connecting rod, the removed objects were then replaced in two different ways. One way is to have a stationary cylinder that is placed in the middle of the crankcase. Since the new cylinder does not move, the overset mesh was also removed. The cylinder was simply subtracted from the volume inside the crankcase instead and the subtract was meshed with the same settings as the crankcase with walls as the boundary conditions for the new cylinder. This model was also set up with a small extra overset mesh volume with interfaces as the previous overset belonging to the crank. An alternative approach is to keep the geometry of the crank as similar to the original as possible. This was achieved in the same way but by using the united crank geometry from the simulation without the connecting rod instead and the overset mesh being kept around it. By running both versions, the impact of the crank geometry could also be evaluated.

4.4 Mesh Modifications

The mesh was coarsened to make the simulations run faster. One approach was to increase the base size of the existing mesh in the entire model. This was done with a base size of 150% compared to the original. Since the flow inside the combustion chamber is of high interest, a setup was also made with a base size of 200% everywhere except in the combustion chamber. In the combustion chamber the mesh was refined to maintain the same size as in the original model. This was done to maintain a high level of accuracy in this part of the model, while still reducing the computational time.

Investigations of the mesh in only the inlet and outlet were also made. Setups with an inlet and outlet mesh of 200%, 250%, and 300% of the original base size were run. The target surface size for the interface between the inlet pipes and the crankcase was reduced to ensure a smoother transition of mesh sizes.

Setups were made with the coarse inlet and outlet, while the crankcase together with the cylinder and exhaust were increased but by a lower percentage. The combustion chamber was kept as the original mesh size for all of these simulations.

The prism layers were also varied in the engine for the mesh with a inlet and outlet at 300% to evaluate the impact of a change in the number of prisms. The total thickness of the prism layers were kept.

How much the mesh can be coarsened is based on the CFL number preferably staying below five, and the y+ values should be under five or above 30 to avoid the overlap/buffer region where there is well defined theory. Since the velocity varies a lot with time, the y+ and CFL values also varies, making it difficult to keep them in the right ranges for the entire simulation. Since the task is to make the simulation run faster, the focus shifted to ensuring that the number of cells in undesirable ranges stayed the same or lower than before. To track this, the number of cells containing a y+ value between five and 30 and the number of cells with a CFL number higher than five are calculated. When changes are made, this can be compared to the original simulation.

4.5 Physics Modifications

The physics setup was modified in a few different ways to conclude if there is something that can be adjusted to minimize the computational time. The time step were increased and a model with only a single component gas was also set up where passive scalars are used to track the gases.

4.5.1 Adaptive Time Step

If a longer time step can be used, this would speed up the simulations significantly. To accomplish this, the adaptive time step module was activated in StarCCM+. Apart from the time stepping, the same setup as for the reference was used. The CFL number was chosen as the time step provider, with a target mean CFL of one and a target maximum CFL of five. The cut-off percentage was tried at 0.5% and 1%. The minimum time step was set to the same as the reference, 0.25 CAD, and the maximum was run at different values ranging from 0.4-0.75 CAD to find a limit for what is tolerable. The maximum change factor was kept at the default, meaning that the time step, at most, could change by a factor of two, between time steps.

Some of the existing reports and measurements were based on a fixed time step. These were adapted to work using a time step-independent definition. The number of time steps for one cycle was measured and used as a variable in reports where necessary. To make the comparison of the results for different setups easier, since the regular simulations all hit exactly 360 CAD each revolution, the adaptive time step models should also do this. The adaptive time step model in the software allows the user to specify checkpoint times that the simulation is required to hit. When approaching a checkpoint, the time step is gradually decreased if necessary. To simplify the mass conservation calculations, it is beneficial if the simulation hits a couple of other timestamps exactly as well, which were also defined here, making it three timestamps in total for each revolution that are predefined.

4.5.2 Single Component Gas Formulation

One setup was made where the multi-component gas was changed to a single gas formulation and a passive scalar were instead used to determine if the gas is fresh fuel mixture or not. This means that the clean air and exhaust gas therefore are undistinguishable from each other. This was not considered an issue since the interesting part is how much of the fresh mixture that is flushed straight through the combustion chamber, as well as the pressures and total mass flows.

To calculate the enthalpy for the gases that are normally present, which are used to compute the heat release during the combustion process, the 7-coefficient NASA polynomials (Eq. 2.42) were used with coefficients from the material database in Star-CCM+. These equations were implemented as field functions since they are dependent on the temperature and then adapted into the combustion model. The theoretical heat release was added as a volumetric energy source inside the combustion chamber to give the temperature increase. Since the gas constant is defined for air in the new model, it was scaled with the molar masses for each gas to achieve the proper enthalpies. To reduce the risk for errors, the computed enthalpies were compared with the ones in the reference model for the initial conditions.

The specific heat of the regular gas mixture varies over the combustion process as the temperature increases and the exchange of molecules occurs. This lead to the specific heat of the single gas being set as a polynomial based on temperature, with coefficients based of an old simulation setup from Husqvarna using a similar concept.

The passive scalar was changed via a scalar source term based on the amount of fuel that would have been burned in each cell if present.

4.6 Postprocessing

The necessary data were extracted from the simulations via reports and scenes. The scenes gave a first visual indication to if the flow behaved as expected. For a more in-depth look at the data, a Python script was created that loads tabulated data from the reports and uses it to plot the data for the reference model as well as for the modified models, for an easy comparison.

To make data of different scales comparable, the MAE was normalized. For this work it was normalized with the mean of the reference data for the different pressures and mass flows, and the normalized MAE (NMAE) is thereby defined by Eq. 4.1.

$$NMAE = \frac{MAE}{mean(A_t)} \tag{4.1}$$

The script computes either the NMAE or the APE of the measurements. When the errors are computed, periods where the data is zero for the reference, for example while a port is closed, are not included in the calculations. For the setups with an adaptive time step, the reference data is interpolated to the time steps of the adaptive model when computing the error.

For the models where the mesh were affected, such as removing and replacing parts in order to remove overset meshes or coarsening the mesh, the mass conservation was closely monitored. For these models the amount of cells with a wall y^+ or CFL number within an undesirable range for each time step were also plotted, to ensure no major mesh related errors are introduced.

4.6.1 Assessing Accuracy

The primary data used to assess the impact of the modifications are:

- Mass-averaged internal pressure inside the crankcase
- Mass-averaged internal pressure inside the combustion chamber
- Mass flow into the combustion chamber
- Mass flow through the Af-, Ah-, and exhaust-port
- λ in the combustion chamber
- Delivery ratio
- Trapping efficiency

Before this could be properly assessed, the simulations first had to be converged. If a simulations is converged or not, was determined by λ, where a change from cycle to cycle of less than 1‰ is considered converged. For the single gas formulation, this could not be done and therefore the mass conservation error is the one determining if it is converged or not.

The DR and TE were retrieved from predefined reports in the model for all cases except the adaptive time steps. If the time step was varied, the DR was instead calculated in Python by integrating the mass flows over time since the reports were defined for a constant time step. The TE defined in Star-CCM+ was still used but with the calculated DR from the script.

Due to the overset meshes being used, it was important to check if the mass was being conserved in the models. This was done separately for the crankcase and the combustion chamber. For the crankcase, the incoming mass was computed through the Af- and Ah-port, and the outgoing mass was computed through the scavenging port. The same was done for the combustion chamber, except that here, the mass into the system was computed through the scavenging port, and the mass out of the system was computed over the exhaust-port. This was done directly in Star-CCM+ by summarizing the mass flows over one entire revolution and calculating the total mass in and out of the chosen control volume.

The mass conservation computation was done in Python for the models with an adaptive time step since the length of each time step varies over the course of one revolution in those simulations. For these, the mass flows for the same ports as above were integrated with respect to the time for both the reference model and the simplified models. These integrals could then be compared instead to determine if the changed model is mass conservative.

4.6.2 Timesavings

The computational time for each simulation gets measured automatically when they are run on the cluster. All final simulation setups for the different simplifications were run with all plot and scene exporting options turned off on the same amount of cores. The time data could then be extracted and compared with respect to the real time elapsed for one revolution. Due to the cluster consisting of several nodes with no manageable way of specifying which ones the simulation will run on, the time can vary slightly depending on which nodes are used. To minimize the risk of obtaining skewed time measurements, the elapsed solver time for each time step was monitored to ensure it did not increase when all exports were turned off.

4.7 Combinations

To combine the different modifications into one model, the mean of the error measurements for the pressures, and the mean for the mass flows was taken for each of the setups. If this mean error were above 5% the setup was not considered for use in any combined model, but the rest were weighted in respect to their timesavings. For each of the main modification categories, the ones with the lowest weighted error were considered for a combined model. If multiple setups of the same type were on par, a conservative approach was taken, where the one with the smaller change in setup was to be used first.

The combined models were then put through the same postprocessing procedure as the individual setups where the error measurements determines if the model is accurate or not. If the results for the combinations gave a good agreement with the reference, a model with a bigger change in setup was tried. The setups were combined two and two at first before they all are combined into one.

5
Results

Using the methods described above, multiple different models were created. The results for all of these simplified models are presented in this chapter for one revolution if nothing else is stated, using a converged solution and compared to a converged revolution from the reference model. The accuracy of the results is quantified using the NMAE and the APE.

5.1 Geometrical modifications

The results for the all the different geometrical changes are presented in this chapter. The data is presented in tables and some plots are included to illustrate the errors during the span of one cycle.

5.1.1 Without Outlet System

This section presents all different setups where the outlet system is removed.

5.1.1.1 Atmospheric Pressure

The NMAE for the different mass flows and pressures can be found in Tab. 5.1 for the setup with the atmospheric pressure as a boundary condition. Almost all of the data deviate significantly from the reference values, giving an overall poor agreement. The pressure inside the combustion chamber gives the best agreement with the reference with a 4% difference.

Table 5.1: The NMAE of the results from the simulation with atmospheric pressure at the outlet.

Data	NMAE [%]
Mass flow Af-port	14.9
Mass flow Ah-port	18.4
Mass flow into exhaust	17.2
Mass flow into CC	16.2
Muffler inlet pressure	110
Crankcase pressure	20.7
CC pressure	4.00

The pressures do not match the reference well, as can be seen in Fig. 5.1–5.2. The pressure at the muffler entry is significantly lower than the reference between approximately 140 and 360 CAD. The pressure inside the crankcase is also lower than the reference during the second half of the cycle.

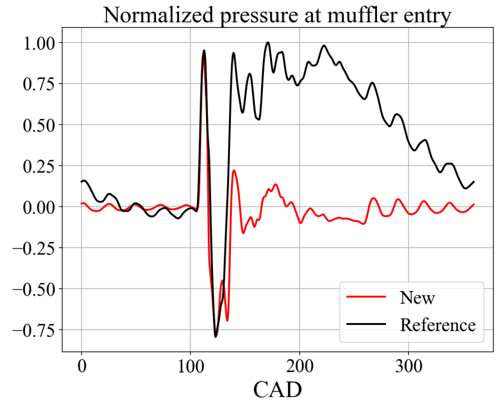

Figure 5.1: Normalized surface-averaged pressure at the muffler entry for the case with atmospheric conditions downstream of the exhaust.

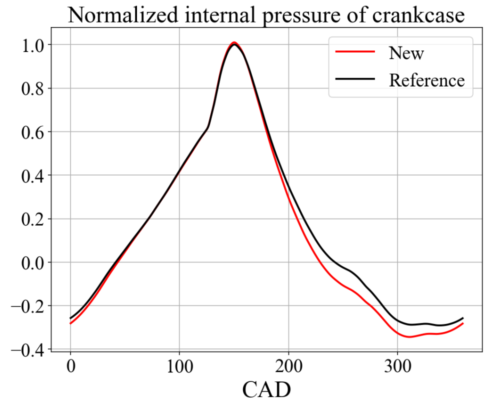

Figure 5.2: Normalized internal pressure inside the crankcase with atmospheric conditions downstream of the exhaust.

The performance parameters, λ, DR, and TE are presented in Tab. 5.2 where the APE is stated with respect to the reference. These also deviate significantly from the reference values.

Table 5.2: The error for the performance parameters of the simulation with atmospheric pressure at the outlet, compared to the reference data.

Parameter	APE [%]
λ	3.13
Delivery ratio	15.7
Trapping efficiency	9.24

In regards to computational time, removing the outlet system and replacing it with a pressure outlet with atmospheric conditions saves about 14.5%. This setup conserves the mass 14.7% better than the reference through the crankcase and 46.1% better through the combustion chamber.

5.1.1.2 Measured Pressure from the Reference

The different types of pressures at the outlet give different levels of correlation to the reference, but all the setups give a better agreement with the reference than using the atmospheric conditions.

Using the volume-averaged pressure from inside the muffler on the boundary, the results in Fig. 5.3-5.4 are obtained. The muffler entry pressure gives a better match than the previous setup, and the crankcase pressure agrees well with the reference pressure.

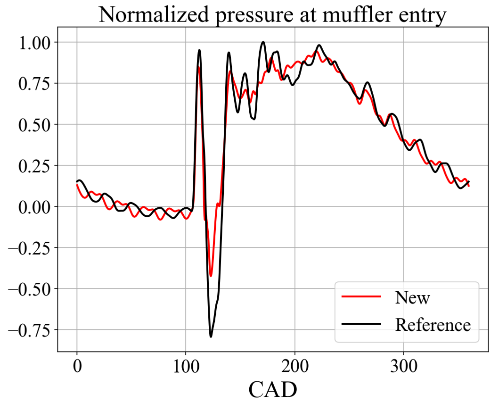

Figure 5.3: Normalized pressure at the muffler entry for the setup with the volume-averaged pressure as the outlet pressure.

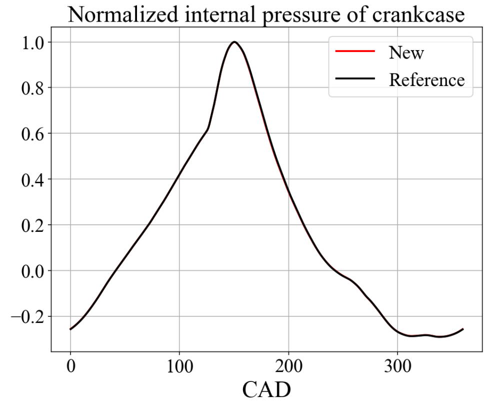

Figure 5.4: Normalized pressure in the crankcase for the setup with the volume-averaged pressure as the outlet pressure.

The NMAE for the results can be found in Tab. 5.3. All values except the pressure at the inlet to the muffler are close to the reference for the setup with the volume-averaged pressure as the boundary condition. The other two pressures, the exit pressure and the entry pressure, give a much worse correlation across the board.

Table 5.3: The NMAE of the results from the simulation with different outlet pressures.

Data	NMAE [%]		
	Volumetric average	Entry pressure	Exit pressure
Mass flow Af-port	0.488	12.6	7.12
Mass flow Ah-port	0.830	15.4	9.04
Mass flow into exhaust	3.84	14.5	9.31
Mass flow into CC	1.53	13.7	8.08
Muffler inlet pressure	17.0	94.1	54.7
Crankcase pressure	0.734	17.2	9.75
CC pressure	0.391	3.37	1.92

The performance parameters λ, DR, and TE are presented in Tab. 5.4. Here it can also be seen that using the volumetric average pressure at the boundary gives quite good results, and that the other two pressures give results that differ more from the reference.

Table 5.4: APE for the performance parameters for the different outlet pressures.

Parameter	APE [%]		
	Volumetric average	Entry pressure	Exit pressure
λ	0.612	2.77	2.03
Delivery ratio	0.165	13.1	7.62
Trapping efficiency	0.404	7.79	4.55

The three different outlet pressures gives an average timesaving of 13.5%, and the mass conservation error is at maximum 2.81% less conservative than the reference for any of the versions.

5.1.2 Removed Inlet

With a removed inlet system, the simulations did not converge within a reasonable amount of time, as can be seen in Fig. 5.5, where λ is decreasing after about nine cycles.

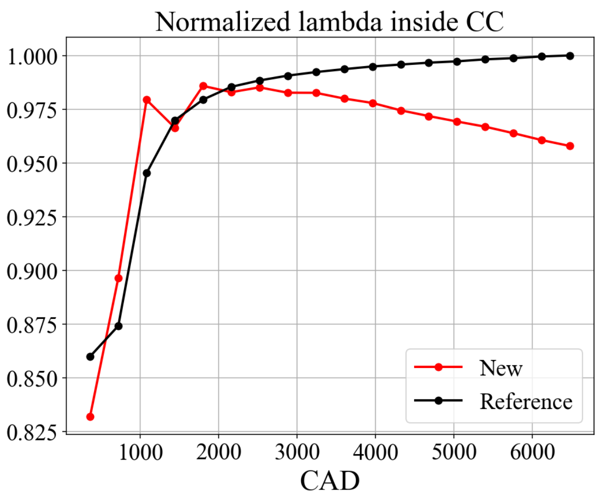

Figure 5.5: λ for the simulation with a removed inlet system.

The results for this simulation is still presented, but for this unconverged simulation. The resulting entry pressure of the muffler is presented in Fig. 5.6 and the internal pressure for the crankcase in Fig. 5.7. Both pressures still give a solid fit, and this is the case for most of the quantities that are extracted further away from the inlet.

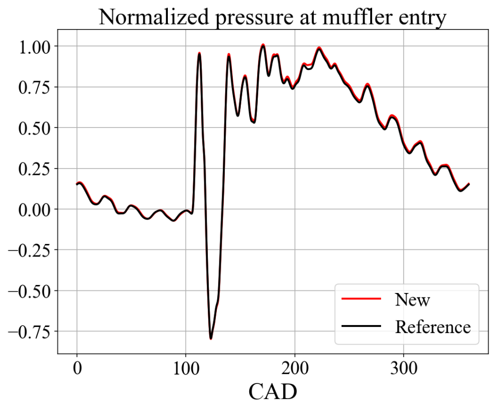

Figure 5.6: The muffler-entry pressure for the setup with the inlet removed.

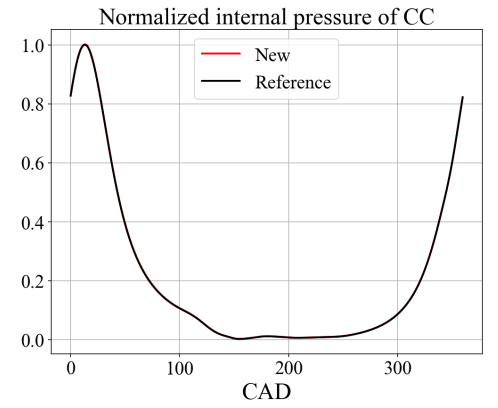

Figure 5.7: The internal pressure inside the combustion chamber for the setup with the inlet removed.

The mass flows through the Af- and Ah-ports are presented in Fig. 5.8 and Fig. 5.9, where they can be seen to be far from the expected mass flows. There is not enough air flowing into the system through the Ah-port during the second half of the cycle, which is then compensated by a too high inflow of fuel mixture at the beginning of the next cycle.

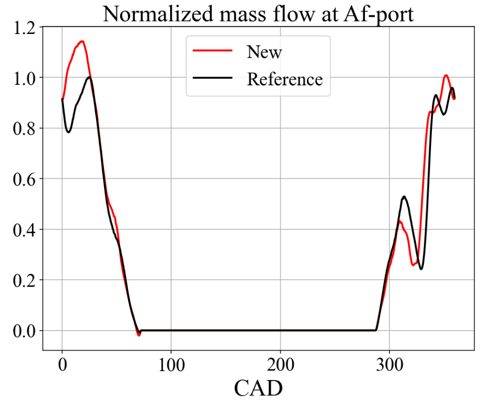

Figure 5.8: Normalized mass flow through the Af-port for the model with the inlet removed.

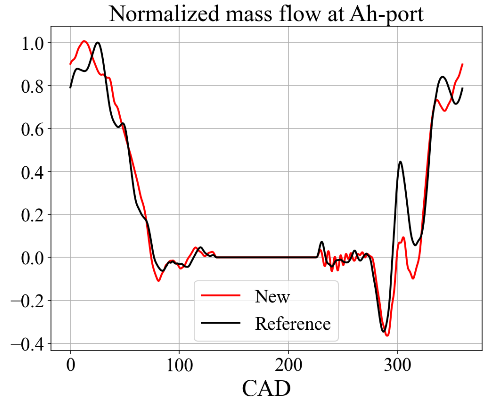

Figure 5.9: Normalized mass flow through the Ah-port for the model with the inlet removed.

The NMAE for the mass flows and pressures can be found in Tab. 5.5. Here it can also be seen that the data extracted far away from the inlet are still decent, but that the ones close to the inlet are far from the reference values.

Table 5.5: The NMAE of pressures and mass flows with the inlet removed.

Data	NMAE [%]
Mass flow Af-port	15.1
Mass flow Ah-port	25.5
Mass flow into exhaust	1.87
Mass flow into CC	2.77
Muffler inlet pressure	2.51
Crankcase pressure	6.84
CC pressure	0.320

The error of the performance parameters are presented in Tab. 5.6. The λ error increases as the simulation continues to run but the error for this revolution is at 4.21%. The DR and TE do not deviate that as much from the reference.

Table 5.6: The error of the performance parameters with the inlet removed compared to the reference data.

Parameter	APE [%]
λ	4.21
Delivery ratio	1.59
Trapping efficiency	0.407

Even though the simulation did not converge, a single cycle run after the presented values are extracted gives a reduction in computational time of 9.66%. The difference in mass conservation is 2.37% better through the crankcase and 3.50% less conservative through the combustion chamber.

5.1.3 Replaced Connecting Rod

Looking at the performance of the simulation when the connecting rod is replaced, it can be seen in Fig. 5.10–5.11 that the pressures agree well with those taken from the reference simulation.

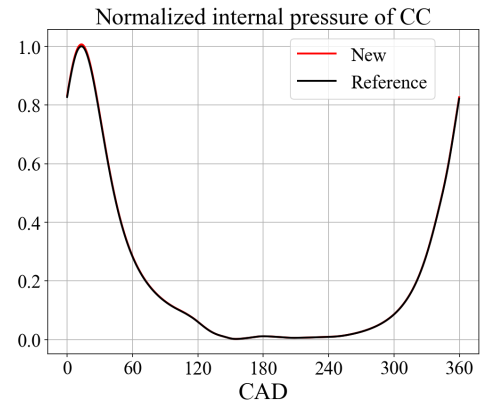

Figure 5.10: Normalized combustion-chamber internal pressure for the simplified model with the connecting rod replaced.

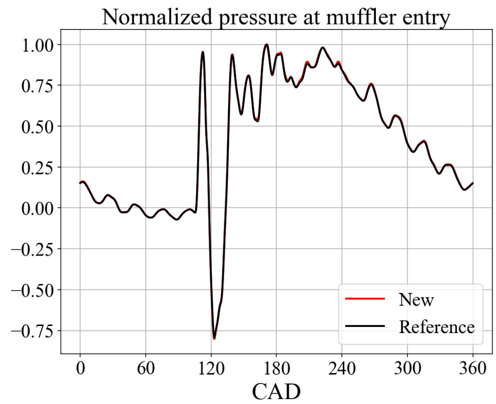

Figure 5.11: Normalized muffler-inlet surface-averaged pressure for the simplified model with the connecting rod replaced.

The data studied to determine the accuracy can be found in Tab. 5.7. The pressures correspond well to the reference data but the mass flows through the Af- and Ah-port are not as close.

Table 5.7: The error of pressures and mass flows when the connecting rod is replaced.

Data	NMAE [%]
Mass flow Af-port	3.85
Mass flow Ah-port	6.24
Mass flow into exhaust	0.877
Mass flow into CC	2.86
Muffler inlet pressure	0.966
Crankcase pressure	2.00
CC pressure	0.655

The error of the performance parameters is presented as the APE with respect to the reference model in Tab. 5.8. All the performance parameters are close to the reference values and differ by less than one percent.

Table 5.8: Error for the performance parameters for the model with the connecting rod replaced.

Parameter	APE [%]
λ	0.561
Delievery ratio	0.762
Trapping efficiency	0.131

A comparison of this setup and the reference in regards to the mass flows through the

Af- and Ah-ports is visualized in Fig. 5.12 and Fig. 5.13. There is a small amount of extra mixture entering the crankcase through the Af-port at the end of the cycle, compensated by a little less mixture entering the crankcase at the beginning of the cycle. The air through the Ah-port also differs from the reference solution, having a slightly different flow profile during the majority of the time the port is open.

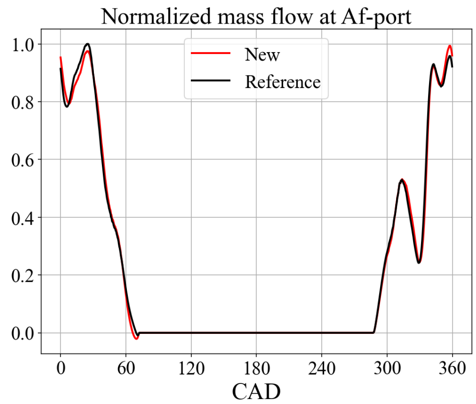

Figure 5.12: Normalized mass flow through the Af-port for the simplified model with the connecting rod replaced.

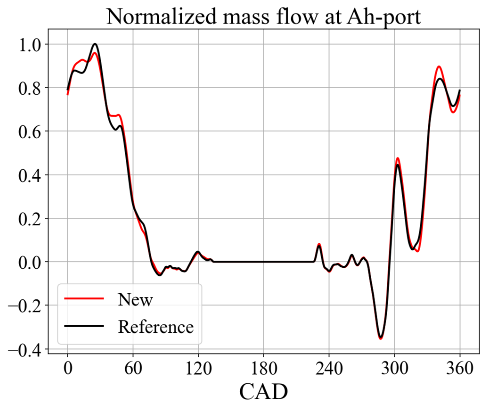

Figure 5.13: Normalized mass flow through the Ah-port for the simplified model with the connecting rod replaced.

The mass conservation error is 7.85% higher in this setup than in the reference through the crankcase, and the mass conservation error through the combustion chamber is 2.79% lower than in the reference. Replacing the connecting rod and thereby removing its overset mesh resulted in a time saving of 21.1%.

5.1.4 Replaced Crank

Some of the resulting pressures from the simulation with the crank replaced can be seen in Fig. 5.14–5.15. The pressure inside the combustion chamber is close to the reference with only a small difference in maximum combustion pressure, and at the muffler entry, it deviates slightly during the second half of the cycle.

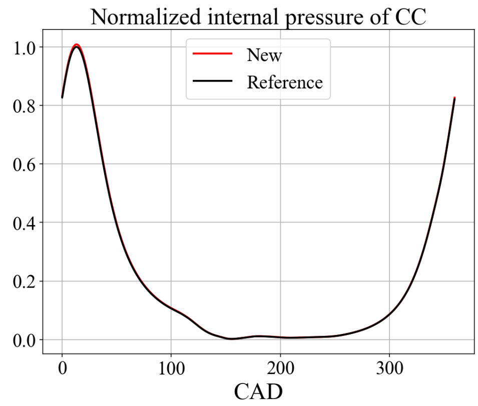

Figure 5.14: Normalized internal pressure of the combustion chamber for the simplified model with the crank replaced.

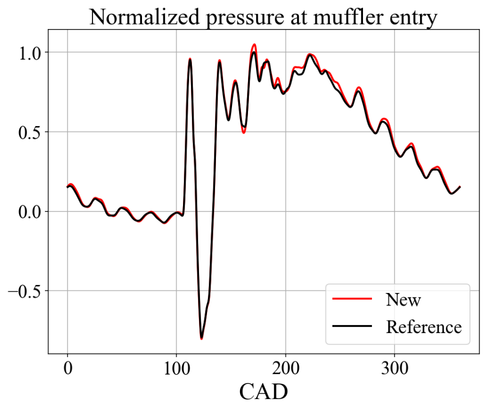

Figure 5.15: Normalized surface-averaged pressure at the inlet to the muffler for the simplified model with the crank replaced.

The error of the performance parameters is presented as the APE with respect to the reference model in Tab. 5.9. No significant change can be seen.

Table 5.9: APE for the performance parameters for the model with the crank replaced.

Parameter	APE [%]
λ	0.415
Delivery ratio	2.27
Trapping efficiency	0.910

The NMAE for the pressures and mass flows can be found in Tab. 5.10, where it can be seen that the pressures match well with the expected result. However, the mass flows deviate a bit more. They differ for the majority of the cycle when the respective ports are open. This can be seen in Fig. 5.16 where the mass flow into the combustion chamber is illustrated.

Table 5.10: The NMAE of results with a replaced crank.

Data	NMAE [%]
Mass flow Af-port	6.09
Mass flow Ah-port	8.11
Mass flow into exhaust	2.62
Mass flow into CC	9.82
Muffler inlet pressure	3.51
Crankcase pressure	2.57
CC pressure	0.877

The peak of the mass flow is greater for the simplified model. The rest of the cycle still matches quite well, however.

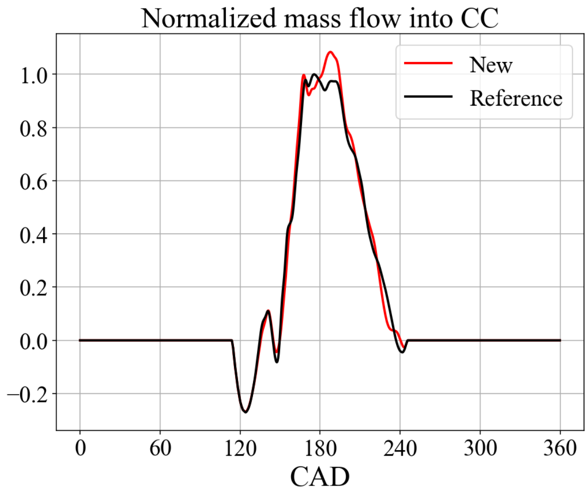

Figure 5.16: Normalized mass flow into the combustion chamber for the simulation with the crank replaced.

The mass conservation differs by 10.4% through the crankcase and 4.58% through the combustion chamber, when compared to the reference. In both of the cases, this model is more mass conservative. Removing and replacing the crank geometry resulted in a time saving of 27.0%.

5.1.5 Replaced Connecting Rod and Crank

When two of the moving parts are made stationary, and only two overset meshes are kept, these being the background and the piston, an error message is triggered stating that cells are outside of a region. The interpolation of the acceptor and donor cells does not work, and the simulation crashes. If the option to treat this error as a warning is activated, the simulation continues to run anyway. This error is most prominent around the time when the piston overset starts to move past the bottom edge of the cylinder volume, but the simulation still manages to converge. Results for a run with this option selected are presented for the geometry with one stationary cylinder. Two different geometries with this option deactivated are also presented, where a small extra overset mesh is utilized to get rid of the error message.

For the single-cylinder setup, with the option "treat error as warning" active, the pressures inside the combustion chamber and at the muffler entry can be seen in Fig. 5.17 and Fig. 5.18 respectively.

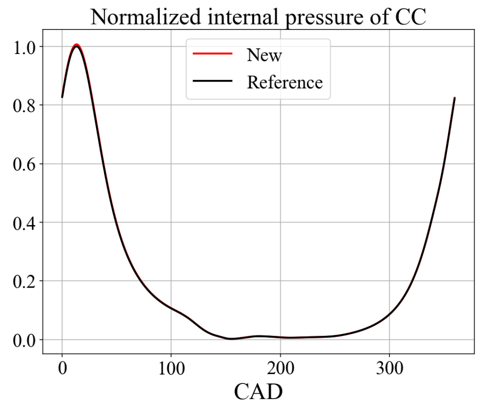

Figure 5.17: Normalized internal pressure of the combustion chamber for the simplified model with the crank and connecting rod replaced, using the option "treat error as warning".

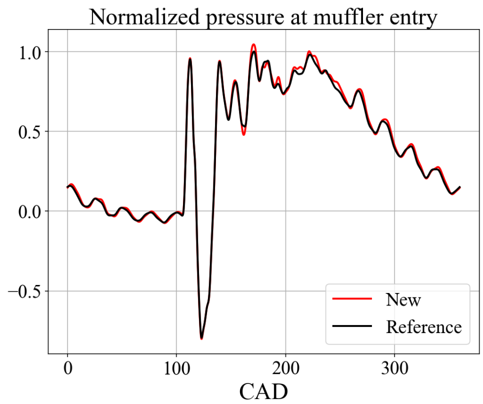

Figure 5.18: Normalized surface-averaged pressure at the inlet to the muffler for the simplified model with the crank and connecting rod replaced using the option "treat error as warning".

The pressure in the combustion chamber matches the reference well, and the pressure at the entry to the muffler is similar to the reference but with a slightly different shape.

For the run with the same geometry with an extra overset mesh, the same graphs are plotted in Fig. 5.19 and Fig. 5.20.

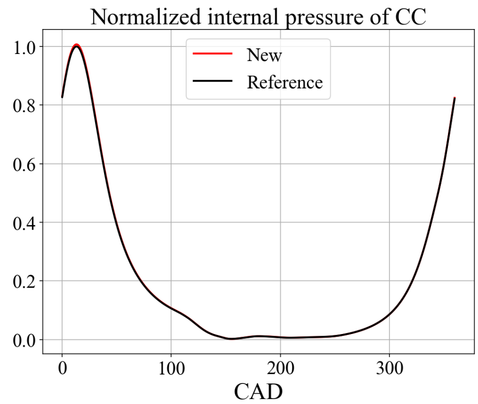

Figure 5.19: Normalized internal pressure of the combustion chamber for the simplified model with the crank and connecting rod removed and replaced with a single cylinder, with an extra overset mesh.

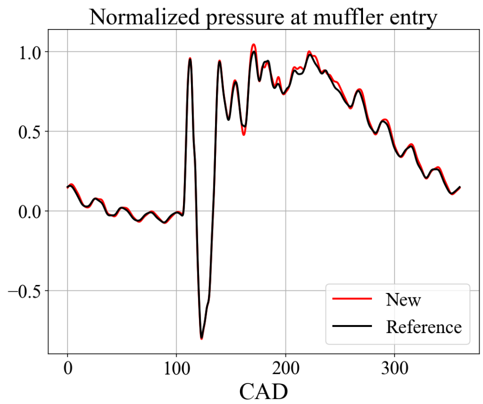

Figure 5.20: Normalized surface-averaged pressure at the inlet to the muffler for the simplified model with the crank and connecting rod removed and replaced with a single cylinder, with an extra overset mesh.

There is no noticeable difference between the graphs with or without the extra overset mesh. This indicates that the error in the simulation that is not utilizing an extra overset does not have any noticeable impact on the results.

The same data for the other geometry, more similar to the original crank with the overset mesh kept, is shown in Fig. 5.21 and Fig. 5.22.

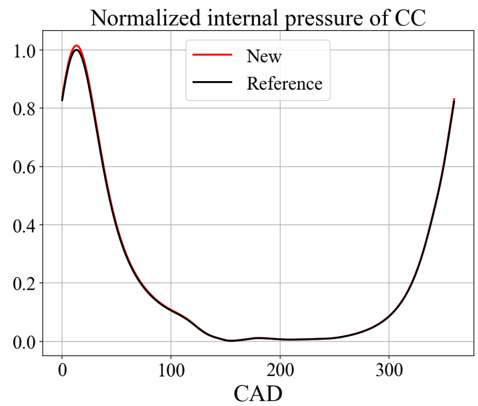

Figure 5.21: Normalized internal pressure of the combustion chamber for the simplified model with a stationary crank from the setup without the connecting rod.

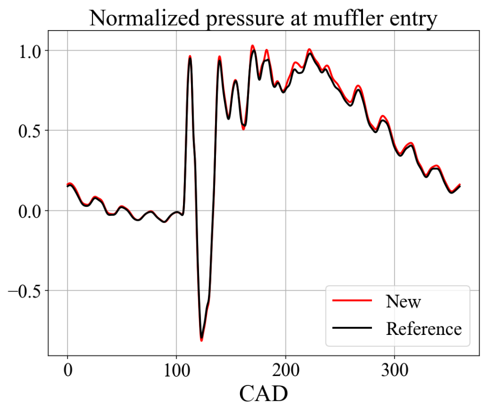

Figure 5.22: Normalized surface-averaged pressure at the inlet to the muffler for the simplified model with a stationary crank from the setup without the connecting rod.

There is a slight difference between the geometries. The overall trends are the same, with the error being a little bit bigger when using the crank from the setup with only the connecting rod replaced. This is clear in Fig. 5.21 where the top pressure is higher for the geometry with the more standard crank geometry than for the ones with a single cylinder. The NMAE for the different setups are presented in Tab. 5.11.

Table 5.11: NMAE for the different cases with the connecting rod and crank replaced.

Data	NMAE [%]		
	Single cylinder	Extra overset	
		Single cylinder	Crank from replaced rod
Mass flow Af-port	6.74	6.81	6.96
Mass flow Ah-port	10.4	10.5	9.20
Mass flow into exhaust	2.32	2.32	3.19
Mass flow into CC	12.0	12.1	9.85
Muffler inlet pressure	3.40	3.40	4.07
Crankcase pressure	3.14	3.35	3.76
CC pressure	0.614	0.625	1.45

Comparing the two simulations with a single cylinder, there is a minimal difference in the errors. The small difference is most likely coming from numerical discrepancies and from the fact that there will always be slight differences between revolutions in the transient simulations. There is a noticeable difference between the two different geometries when looking at the errors. The pressures can be seen to differ more from the reference, but the mass flows are more accurate overall.

The performance parameters are presented in Tab. 5.12. The λ value differs between the three setups, but the two single-cylinder geometries still give similar results. The more accurate shape of the crank gives a noticeably lower error for λ but is further from the reference for the delivery ratio.

Table 5.12: APE for the performance parameters with the connecting rod and crank replaced.

Parameter	APE [%]		
	Single cylinder	Extra overset	
		Single cylinder	Crank from replaced rod
λ	1.90	2.22	0.458
Delivery ratio	2.07	1.95	2.81
Trapping efficiency	0.909	0.879	0.803

The mass conservation errors for the different setups are presented in Tab. 5.13. There is a major difference between the setups, where the case with no overset and the small overset is more conservative than the one with the overset over the entire new part replacing the crank and connecting rod. It should be noted that a negative value for the mass conservation difference indicates that it is better than the reference, and a positive value that it is worse.

Table 5.13: Mass conservation error compared to the reference with the connecting rod and crank replaced.

Difference in mass conservation	Single cylinder	Extra overset	
		Single cylinder	Crank from replaced rod
Crankcase [%]	-93.2	-93.1	+18.8
CC [%]	+11.0	+3.40	-9.19

Replacing both the connecting rod and the crank with a single stationary cylinder, the time saved is 38.7%. When adding a small extra overset, the time saved is reduced to 34.9%. By using the geometry closer to the original crank, with the larger overset mesh, the time saving was 21.2%.

5.2 Mesh Modifications

The results for the coarsened meshes are presented in this chapter. Results have been divided into different categories. One section presents a coarsening of the mesh for the inlet and outlet, one for the entire engine, and one section for modified prism layers. The results for combined meshes with different base sizes are also presented.

5.2.1 Inlet and Outlet

An increased base size of the mesh inside the inlet and outlet gave a good agreement with the reference for all the versions. The pressures can be seen for the 300% base size case in Fig. 5.23 and Fig. 5.24.

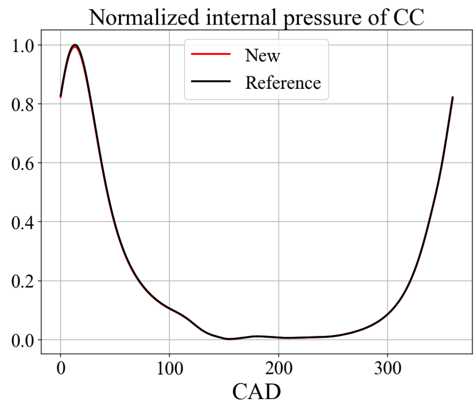

Figure 5.23: Normalized internal pressure of the combustion chamber for the simplified model with the 300% coarsened inlet and outlet.

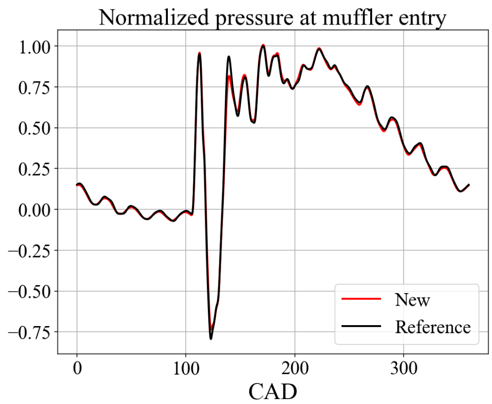

Figure 5.24: Normalized surface-averaged pressure at the inlet to the muffler for the simplified model with with the 300% coarsened inlet and outlet.

The number of elements where y^+ is between 5 and 30 is presented in Fig. 5.25 and where CFL is above 5 in Fig. 5.26, these are also for the 300% mesh. Both of the them are slightly lower than in the reference case.

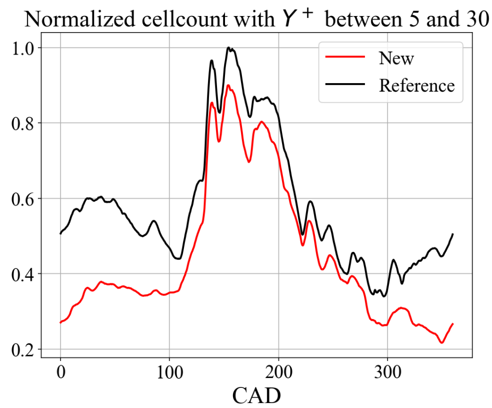

Figure 5.25: The number of elements where y+ is between 5 and 30 presented with respect to CAD.

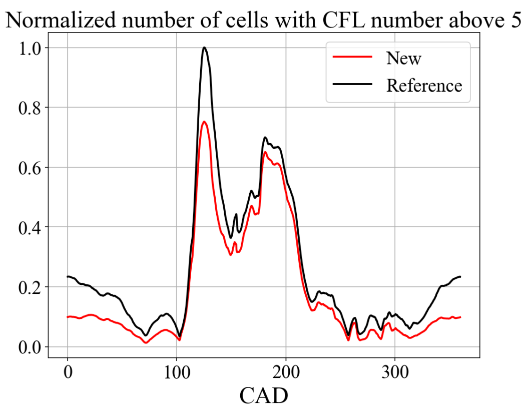

Figure 5.26: The number of elements where CFL is above 5 presented with respect to CAD.

The NMAE for the results can be found in Tab. 5.14. The results for each base size of the mesh in the inlet and outlet are presented in the same table for an easy comparison. In general, the coarser the mesh is, the larger the error becomes.

Table 5.14: The NMAE of the pressures and mass flows with changed base sizes for the inlet and outlet.

Data	NMAE [%]		
	With base size:		
	200%	250%	300%
Mass flow Af-port	1.25	2.11	2.61
Mass flow Ah-port	2.03	3.92	4.16
Mass flow into exhaust	0.563	1.17	1.45
Mass flow into CC	0.583	1.27	1.61
Muffler inlet pressure	3.84	4.86	3.13
Crankcase pressure	1.51	3.79	4.23
CC pressure	0.330	0.694	0.676

The APE for the performance parameters are presented for all the mesh sizes in Tab. 5.15. All setups give an overall low error.

Table 5.15: APE for the performance parameters for the different base sizes on the mesh in the inlet and outlet.

Parameter	APE [%]		
	With base size:		
	200%	250%	300%
λ	0.348	0.532	0.282
Delivery ratio	0.469	1.18	1.49
Trapping efficiency	0.124	0.390	0.515

In Tab. 5.16, the timesavings for the coarse inlets and outlets, as well as the mass conservation in comparison to the reference can be seen. The timesavings do not differ significantly but the mass conservation improves slightly for the coarser mesh.

Table 5.16: Timesavings and mass conservation for different mesh sizes in the inlet and outlet.

Mesh size of inlet and outlet	200%	250%	300%
Timesavings [%]	14.7	15.5	16.8
Difference crankcase [%]	3.66	-0.0200	-4.67
Difference CC [%]	-4.45	0.474	-2.58

5.2.1.1 Prism Layers in 300% Base Size for Inlet and Outlet

The model with 300% of the base size in the inlet and outlet is modified with fewer prism layers in the exhaust and crankcase. In Tab. 5.17, the results with different changes of the prism layers are presented. Some of the values are better with fewer prism layers, such as the mass flows through the Ah- and Af-ports, but the internal pressure of the crankcase is significantly worse. The pressure inside the combustion chamber is close to the reference for the setup with one less prism layer, and is still good with two prism layers removed in the combustion chamber.

Table 5.17: The NMAE of the results with changed prism layers.

Data	NMAE [%]	
	Nr of prism layers removed	
	1	2 in CC 1 in Crc & exhaust
Mass flow Af-port	2.26	4.24
Mass flow Ah-port	3.40	6.15
Mass flow into exhaust	1.99	1.29
Mass flow into CC	2.47	1.68
Muffler inlet pressure	3.22	3.22
Crankcase pressure	7.62	6.31
CC pressure	0.29	1.08

The errors for the performance parameters show that the values are close to the reference as can be seen in Tab. 5.18, but removing one prism layer did increase the error compared to the original 300% base mesh.

Table 5.18: APE for the performance parameters for the different prism layers.

Parameter	APE [%]	
	Nr of prism layers removed	
	1	2 in CC 1 in Crc & exhaust
λ	1.04	2.25
Delivery ratio	2.30	1.01
Trapping efficiency	0.514	0.718

The mass conservation through the crankcase is 73.1% better than the reference, and the combustion chamber is 44.2% better than the reference with one less prism layer. The timesaving becomes 20.7% compared to the reference. Removing an additional prism layer in the combustion chamber only saves an additional 0.1 percentage points, for a total timesaving of 20.8%.

5.2.2 Entire Engine

When the base size of the mesh is increased in the entire engine, the number of elements in undesirable y^+ and CFL ranges decreases noticeably. The number of elements where y^+ is between 5 and 30 is presented in Fig. 5.27 and where the CFL number is above 5 in Fig. 5.28.

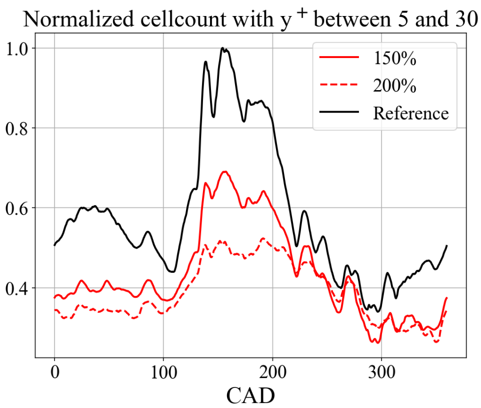

Figure 5.27: The number of elements where y$^+$ is between 5 and 30 presented with respect to CAD, with an increased base size in the entire engine.

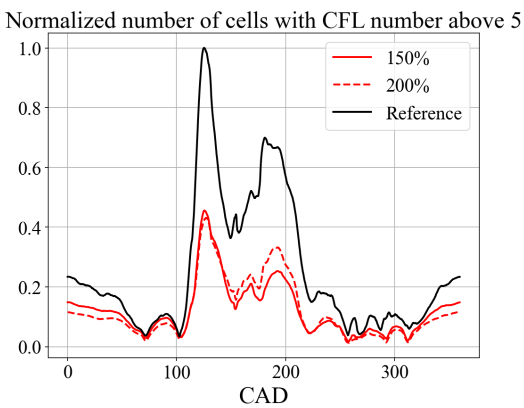

Figure 5.28: The number of elements where CFL is above 5 presented with respect to CAD, with an increased base size in the entire engine.

The errors are presented in Tab. 5.19 for the case with a base size of 150% compared to the original mesh and for the case with 200% of the original, but with the combustion chamber kept at the original mesh size. This is due to the poor performance inside the combustion chamber when using the 150% mesh everywhere. Especially the pressure in the combustion chamber correlates better when reverting to the original size. All of the errors increases when increasing the mesh size, the difference is biggest for pressure at the inlet to the muffler, with a deviation from the reference of 7.70%.

Table 5.19: NMAE for the performance parameters for the different base sizes.

Data	NMAE [%] With base size: 150%	NMAE [%] With base size: 200% original CC
Mass flow Af-port	1.41	1.96
Mass flow Ah-port	2.27	3.39
Mass flow into exhaust	1.98	2.68
Mass flow into CC	3.10	3.97
Muffler inlet pressure	5.12	7.70
Crankcase pressure	5.92	6.05
CC pressure	1.81	0.440

The error for the performance parameters are presented in Tab. 5.20. It can be seen that the coarser mesh gives a higher error for λ and the trapping efficiency whereas the delivery ratio is similar.

Table 5.20: APE for the performance parameters for the different base sizes.

Parameter	APE [%]	
	With base size:	
	150%	200% original CC
λ	1.88	3.46
Delivery ratio	2.31	2.80
Trapping efficiency	0.0106	1.31

The simulation with 150% of the original base size give a 40.4% timesaving and the one with 200% of the original base size, a 50.3% timesaving. The mass conservation through the crankcase is 87.6% better for the 150%, and 86.3% better for the 200%. Through the combustion chamber, the mass conservation is 79.5% better for the 150%, and 70.8% better for the 200%.

5.2.3 Combined Mesh Changes

Here are the results from meshes that have one base size for the inlet and outlet systems and another base size for the core of the engine, excluding the combustion chamber which is kept at the original mesh size. When referencing the different setups, the first base size percentage represents the base size in the core of the engine and the second percentage the base size in the inlet and outlet, in relation to the original size.

For two of the setups, the number of elements where y^+ is between 5 and 30 is presented in Fig. 5.29 and where CFL is above 5 in Fig. 5.30. It can be seen that both the y^+ values and the CFL numbers are better with the new mesh sizes.

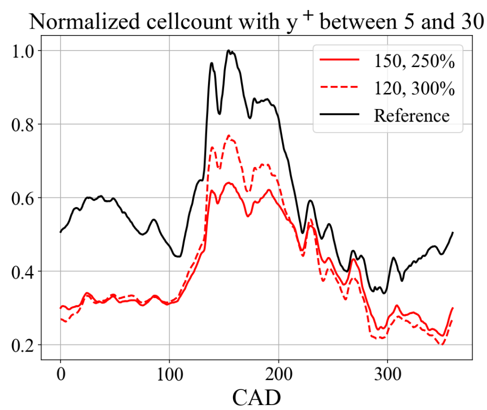

Figure 5.29: The number of elements where y^+ is between 5 and 30 presented with respect to CAD for the mesh using 120, 300% and 150, 250%.

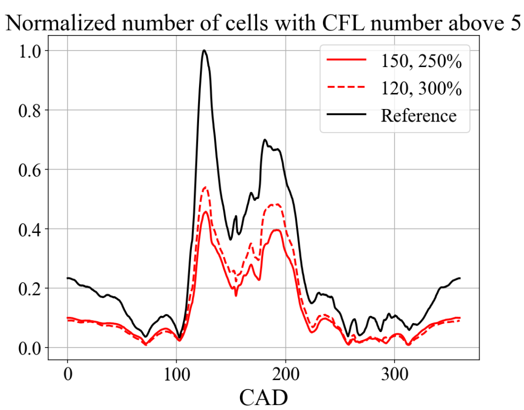

Figure 5.30: The number of elements where CFL is above 5 presented with respect to CAD for the mesh using 120% and 300% and 150, 250%.

The pressure at the muffler entry is presented in Fig. 5.31–5.32 for the 120, 300%

mesh and the 150, 250% mesh. There is a clear difference between the two, where the simulation with a coarser core mesh deviates more from the reference pressure.

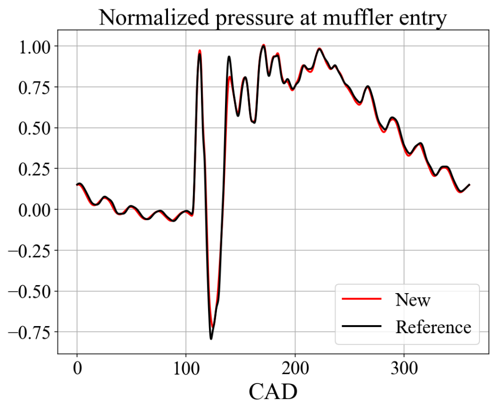

Figure 5.31: Pressure at the muffler entry for the 120, 300% mesh.

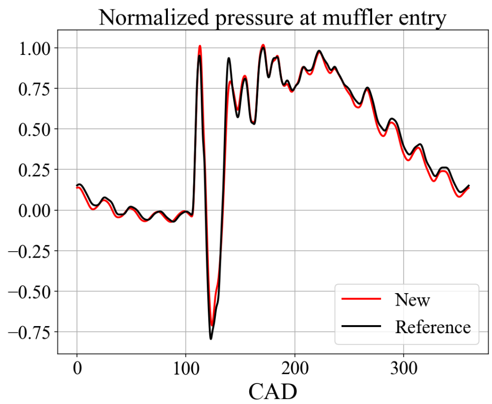

Figure 5.32: Pressure at the muffler entry for the 150, 250% mesh.

The mass flow into the combustion chamber also differs between the 120, 300% and the 150, 250% mesh as can be seen in Fig. 5.33 and Fig. 5.34. The shape is the same but the error is prominent for the coarser core mesh.

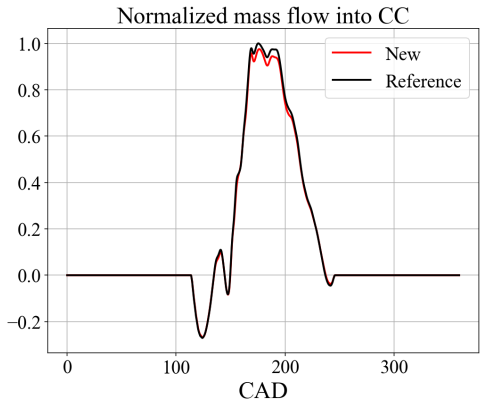

Figure 5.33: Mass flow into the combustion chamber for the 150, 250% mesh.

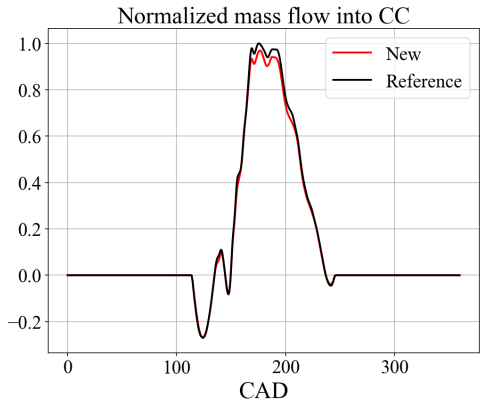

Figure 5.34: Mass flow into the combustion chamber for the 200, 250% mesh.

The NMAE for the pressures and mass flows can be found in Tab. 5.21. From the numbers, it can be seen that the mesh size in the core of the engine has the biggest impact on the accuracy of the results.

Table 5.21: The NMAE of results with different base sizes for the inlet/outlet, and the rest of the engine.

Data	NMAE [%]		
	With base size:		
	120% & 300%	150% & 250%	200% & 250%
Mass flow Af-port	2.38	2.28	2.62
Mass flow Ah-port	3.62	3.98	4.83
Mass flow into exhaust	2.37	2.72	3.39
Mass flow into CC	2.92	3.46	4.78
Muffler inlet pressure	3.91	7.29	8.51
Crankcase pressure	7.96	8.00	7.33
CC pressure	0.532	0.524	0.64

The APE for the performance parameters are presented for all the mesh sizes in Tab. 5.22. The accuracy of λ and the DR is clearly decreasing as the mesh is coarsened with the highest error being 3.70% for the DR.

Table 5.22: APE for the performance parameters with different base sizes for the inlet/outlet, and the rest of the engine.

Parameter	APE [%]		
	With base size:		
	120% & 300%	150% & 250%	200% & 250%
λ	1.64	2.47	3.44
Delivery ratio	2.41	2.61	3.70
Trapping efficiency	1.03	0.917	1.60

The timesavings and the mass conservation comparison for the different setups can be found in Tab. 5.23. A coarser mesh, yields a faster simulation time, although at the cost of accuracy. But the mass conservation is good in all of the versions.

Table 5.23: Timesavings for different mesh sizes.

Mesh sizes	120% & 300%	150% & 250%	200% & 250%
Timesavings [%]	38.7	42.8	52.2
Difference crankcase [%]	-70.1	-76.2	-73.9
Difference CC [%]	-24.2	-39.6	-80.6

5.3 Modifications of the Physical Setup

The results of the different modifications related to the physics of the simulation is presented in two sections, with the first being the time discretization and the second the single gas formulation.

5.3.1 Adaptive Time Step

When using two different cutoffs for the time step provider, 0.5% and 1%, both simulations give good results. The 0.5% cutoff gives slightly more accurate results but takes a bit longer to run since it takes shorter time steps on average, see App. A for graphs. Since the 1% still gives acceptable results, this is the cutoff percentage that is used for all adaptive time step models.

Using the maximum time step of 0.5 CAD, the pressures agree well compared with the original model, as can be seen in Fig. 5.35–5.36.

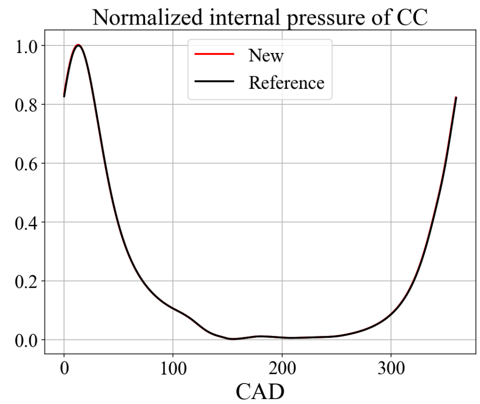

Figure 5.35: Normalized internal pressure of the combustion chamber for the model using a maximum adaptive time step of 0.5 CAD.

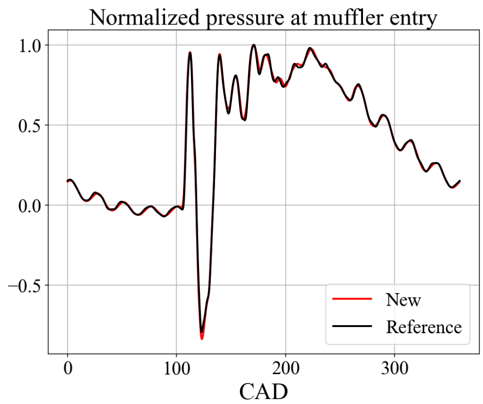

Figure 5.36: Normalized surface-averaged pressure at the inlet to the muffler using a maximum adaptive time step of 0.5 CAD.

For all different maximum time steps, the NMAE for the results are presented in Tab. 5.24. The overall trend for the majority of data, is that a longer time step results in slightly larger errors. The pressure at the inlet to the muffler is the one with the largest error when the time step is increased.

Table 5.24: The NMAE of the data when different maximum time steps are used.

Data	NMAE [%]			
	Maximum step size [CAD]:			
	0.4	0.5	0.6	0.75
Mass flow Af-port	1.69	2.19	3.12	3.84
Mass flow Ah-port	2.16	2.88	3.82	4.47
Mass flow exhaust-port	1.05	1.28	1.38	1.42
Mass flow into CC	2.07	2.83	2.99	3.02
Muffler inlet pressure	2.30	3.57	4.85	6.39
Crankcase pressure	0.83	1.06	1.01	1.00
CC pressure	0.44	0.382	0.500	0.528

The APE for the performance parameters can be found in Tab. 5.25, they all have an error below one percent for all of the maximum time step sizes.

Table 5.25: APE for the performance parameters with different maximum time steps.

Parameter	APE [%]			
	Maximum step size [CAD]:			
	0.4	0.5	0.6	0.75
λ	0.219	0.245	0.209	0.0653
Delivery ratio	0.0558	0.112	0.112	0.156
Trapping efficiency	0.139	0.158	0.184	0.174

The timesavings for the different setups are summarized in Tab. 5.26, together with the difference in mass conservation. It can be seen that the amount of time saved starts to flatten out with the timestep increase. It should also be noted that the mass conservation error through the crankcase increases significantly with larger time steps, although the absolute error is, however, still within an acceptable range.

Table 5.26: Timesavings for different maximum time step sizes.

Maximum step size [CAD]	0.4	0.5	0.6	0.75
Timesavings [%]	37.5	47.7	53.4	59.0
Difference crankcase [%]	+9.01	+15.5	+19.6	+25.3
Difference CC [%]	–6.77	–7.327	–5.99	–5.79

In Fig. 5.37, the time step size taken by the simulation with a maximum step size of 0.6 CAD can be seen over one cycle.

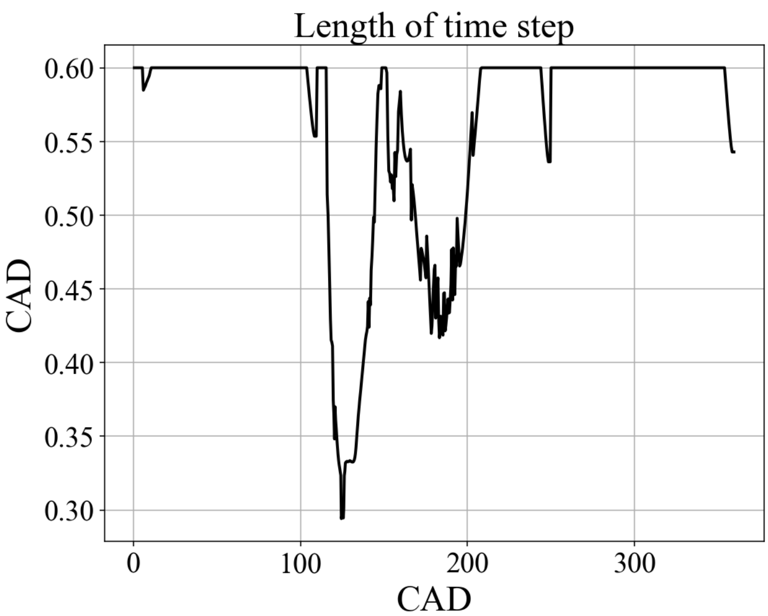

Figure 5.37: Time step size for one cycle with a maximum step size of 0.6 CAD.

The time step can be seen to shorten as the scavenging port opens. Shorter time step valleys can also be seen just after 100 CAD, around 250 CAD, and leading up to 360 CAD. These are due to user input where it was desirable for the simulation to hit a few exact timestamps to simplify some of the report definitions.

5.3.2 Single Component Gas Setup

The simulation setup for the single component gas, with passive scalars to track the flow was not able to be properly setup in the allotted time. The main issue is that the temperature, and therefore the pressure, never reaches the correct values in the combustion chamber which can be seen in Fig. 5.38. Due to this, the results will be incorrect. Some of the reports have not yet been properly defined for the new fluid setup such as the trapping efficiency and λ, meaning that there is no way of knowing how these are affected by the changes. This does not mean that the work was done in vein, as the simulation can still give an indication of the potential timesaving, given proper time to get everything working as intended.

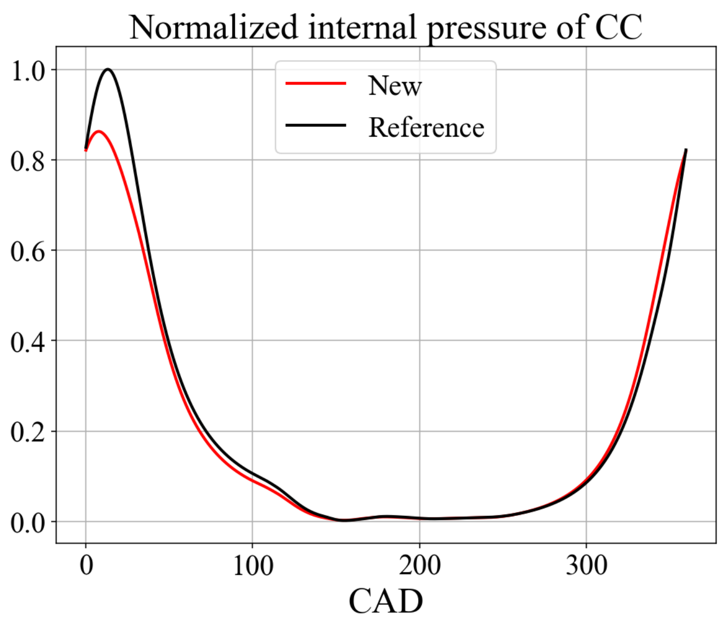

Figure 5.38: Pressure in the combustion chamber for the simulation with a single gas formulation.

The shape of the mass flow at the exhaust looks promising as can be seen in Fig. 5.39, but the magnitude is off compared to the reference.

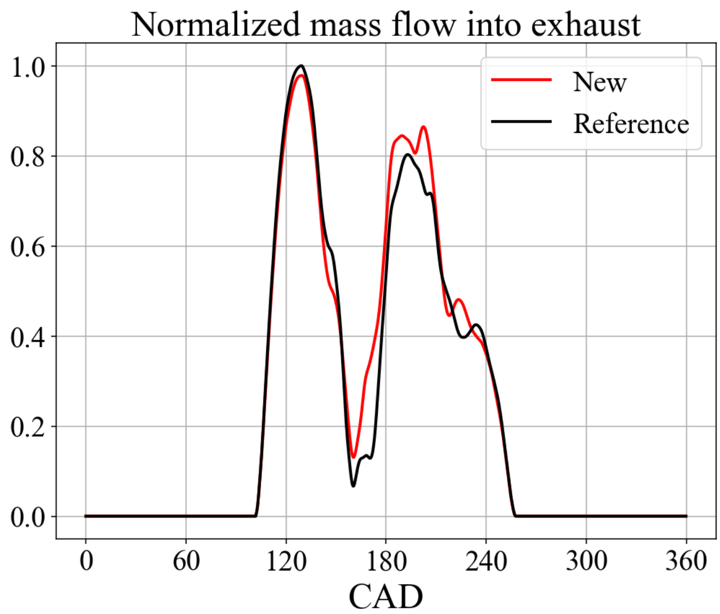

Figure 5.39: Mass flow through the exhaust for the simulation with a single gas formulation.

The NMAE for the pressures and mass flows can be found in Tab. 5.27. All of the data deviates significantly from the reference values, giving an overall poor agreement.

Table 5.27: The NMAE of the results from the simulation with the single gas formulation.

Data	NMAE [%]
Mass flow Af-port	7.13
Mass flow Ah-port	20.5
Mass flow into exhaust	10.1
Mass flow into CC	31.6
Muffler inlet pressure	14.0
Crankcase pressure	25.1
CC pressure	11.0

The APE of λ, DR and TE are presented in Tab. 5.28 where the APE is stated with respect to the reference. Only the DR is properly defined at the moment with one passive scalar, which is the reason the other are left empty.

Table 5.28: The error of the performance parameters with a single gas formulation.

Parameter	APE [%]
λ	-
Delivery ratio	12.0
Trapping efficiency	-

The current setup gives at a timesaving of 38.1%. The mass conservation error is 15.5% better through the crankcase compared to the reference, and 33.9% better through the combustion chamber.

5.4 Result Summary

The mean errors for the pressure and the mean error for the mass flows are presented for each of the modifications in Tab. 5.29. The models with mean errors above 5% are not used for the combined models.

Table 5.29: A summary of the results from all of the modifications.

Simulation setup	Average error [%]		Timesavings [%]
	Pressure	Mass flow	
Atmospheric pressure outlet	45.2	16.7	14.5
Volume avg pressure outlet	6.03	1.67	12.4
Muffler entry pressure outlet	38.2	14.0	14.8
Muffler exit pressure outlet	22.1	8.39	13.4
Removed inlet system	3.22	11.3	9.66
Replaced connecting rod	1.21	3.46	21.1
Replaced crank	2.32	6.66	27.0
Stationary crank, added cylinder	3.10	7.30	21.2
Stationary cylinder only, extra overset	2.46	7.93	34.9
Stationary cylinder only	2.39	7.88	38.7
200% inlet and outlet mesh	1.89	1.11	14.7
250% inlet and outlet mesh	2.12	3.11	15.5
300% inlet and outlet mesh	2.68	2.46	16.8
1 less prism layer	3.71	2.53	20.7
1 less prism in core, 2 less in CC	3.53	3.34	20.8
150% base size	4.28	2.19	40.4
200% base size	4.73	3.00	50.3
120% core and 300% in and out	4.14	2.82	38.7
150% core and 250% in and out	5.27	3.11	42.8
200% core and 250% in and out	5.49	3.91	52.2
Adaptive time step 0.4 CAD	1.19	1.74	37.5
Adaptive time step 0.5 CAD	1.67	2.29	47.7
Adaptive time step 0.6 CAD	2.12	2.83	53.4
Adaptive time step 0.75 CAD	2.64	3.19	59.0
Single component gas	16.7	17.3	38.1

The versions corresponding better with the reference are presented in Tab. 5.30, where the mean errors have been weighted by their respective timesavings for one revolution.

Table 5.30: A summary of the errors from all of the modifications within the acceptable error margin, weighted by their respective timesavings.

Simulation setup	%Error per %time saved [-]	
	Pressure	Mass flow
Replaced connecting rod	0.0573	0.164
200% inlet and outlet mesh	0.129	0.0754
250% inlet and outlet mesh	0.137	0.201
300% inlet and outlet mesh	0.159	0.146
1 less prism layer	0.179	0.122
1 less prism layer in core, 2 less in CC	0.170	0.160
150% mesh size increase	0.106	0.0542
200% base size	0.0941	0.0596
120% core mesh and 300% in and out	0.107	0.0728
Adaptive time step 0.4 CAD	0.0318	0.0464
Adaptive time step 0.5 CAD	0.0351	0.0481
Adaptive time step 0.6 CAD	0.0397	0.0530
Adaptive time step 0.75 CAD	0.0447	0.0540

5.5 Combinations

The combined models are made from the simulations with the replaced connected rod, the mesh with 120 % base size inside the crankcase and exhaust and 300% in the inlet and outlet, with the combustion chamber at original size, and utilizing adaptive time stepping.

The results for all the combined setups are presented in Tab. 5.31.

Table 5.31: The NMAE of the results for the combined setups.

Data	NMAE [%]			
	No rod 120,300%	Adaptive 0.4 120,300%	Adaptive 0.5 No rod	Adaptive 0.6 No nod 120,300%
Mass flow Af-port	3.90	2.77	4.53	4.34
Mass flow Ah-port	6.38	3.63	7.02	6.33
Mass flow into exhaust	1.46	2.00	1.42	1.71
Mass flow into CC	3.12	3.59	4.33	4.18
Muffler inlet pressure	3.48	4.46	3.47	5.11
Crankcase pressure	7.46	7.50	2.27	6.60
CC pressure	0.176	0.507	0.865	0.480

For the model without the connecting rod and the modified mesh, most of the errors are below 5%. Only the errors for the mass flow into the Ah-port and the crankcase pressure are above. For the combination with a maximum time step of 0.4 CAD and the mesh, the crankcase pressure is above 5%. For the combination of the adaptive time step and no connecting rod, only the mass flow through the Ah-port was above 5% and the mass flow into the exhaust was better than in any of the other combinations. For the model with all of the different simplification types combined, the results show no significant difference compared to the results from the separate combinations, they are even better in some cases. The performance parameters are presented in Tab. 5.32 where all of the models give relatively small errors.

Table 5.32: Performance parameters for the combined models.

Parameter	APE [%]			
	No rod 120,300%	Adaptive 0.4 120,300%	Adaptive 0.5 No rod	Adaptive 0.6 No rod 120,300%
λ	0.545	1.19	0.624	1.19
Delivery ratio	1.05	2.26	0.667	1.31
Trapping efficiency	0.541	1.14	0.0187	0.873

For the final combination with a replaced connecting rod, a coarser mesh, and an adaptive time step with a maximum of 0.6 CAD, the mass conservation error is 6.62% better for the crankcase and 16.8% better for the combustion chamber. This setup gives a timesaving of 68.3%.

5.6 Final Setup

The final setup is the combination of the adaptive time step with a maximum time step of 0.6 CAD, the connecting rod replaced and the 120, 300% mesh. This results in a computational time that is 68.3% shorter than the reference, where the average error is 4.14% for the mass flows and 4.06% for the pressures. The internal pressure in the combustion chamber can be seen in Fig. 5.40 and the crankcase pressure in Fig. 5.41.

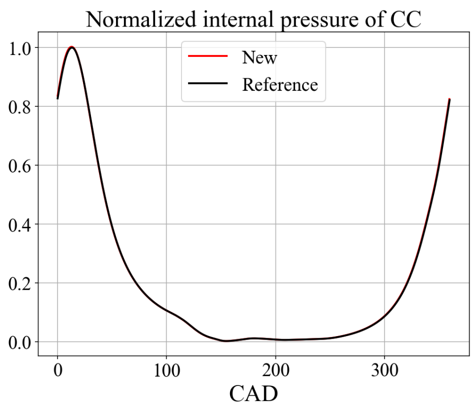

Figure 5.40: Normalized internal pressure of the combustion chamber for the final setup.

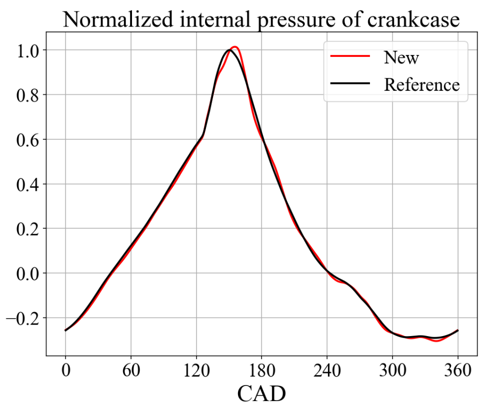

Figure 5.41: Normalized internal pressure inside the crankcase for the final setup.

The data that has the highest error is the pressure inside the crankcase, which can be seen to correspond quite well with the reference, the difference being the maximum pressure which is slightly higher.

The mass flows into the combustion chamber and into the exhaust are close to the reference as can be seen in Fig. 5.42 and Fig. 5.43. The three remaining graphs can be found in App. B.

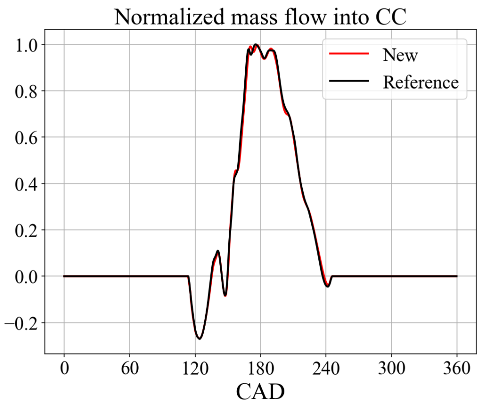

Figure 5.42: Normalized mass flow into the combustion chamber for the final setup.

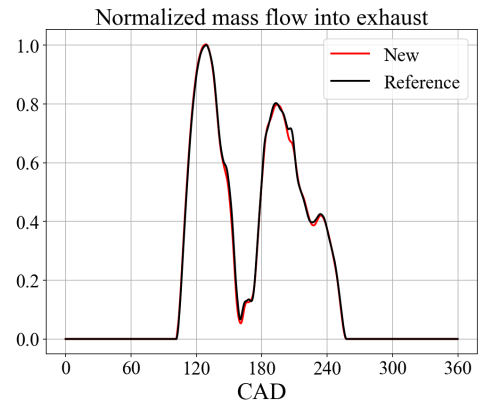

Figure 5.43: Normalized mass flow into the exhaust for the final setup.

6
Conclusion

The aim of the thesis was to develop a simplified model of a two-stroke engine to decrease the computational time. This was done by investigating three main categories of simplifications, these being the geometry, the mesh and the physics setup of the model. The goal was to reduce the time for one cycle by 50% without compromising the accuracy of the results too much which the final setup achieved.

The models where the inlet and outlet are removed are dependent on data for the properties of the flow at the inlet and outlet, which means that there is a need for an equivalent converged solution before these simulation setups can be utilized properly. This makes these changes valid only when working with designs that already have data from previous simulations. They would not work as well for changes in the design since the boundary conditions would have to be altered for the simulation to produce correct results. The removed outlet could be used for extracting data when the simulation has already converged, but since the setup without the inlet never converged for the λ value, this should not be used. This could be due to the boundary condition being set too close to the volume of interest and giving numerical errors.

The version where the connecting rod has been replaced is more useful for design iterations since it has been shown that the model behaves in more or less the same way if it is removed. The movement of the crank, on the other hand, seems to be more important for the flow since the results become inaccurate when it is made stationary. Therefore, it is preferred to keep the crank as a moving part, since the movement drives the flow to some extent. However, removing the connecting rod might not be preferable if changes are made to the bottom of the piston or to the crank since they are connected and could influence each other. Furthermore, removing the connecting rod might not be preferable if changes are made to the angle or the geometry of the Af-inlet, since the incoming gas will hit the rod differently as it enters the crankcase.

From the mesh simulations, the conclusion is that the mesh inside the crankcase could not be coarsened much, since this increased the errors significantly. If the geometry of the crankcase is to be changed, a coarsened mesh could produce accurate results, but it might be preferable to revert back to the original mesh configuration to fully assess the impact of the new geometries. The prism layers also had a noticeable impact on the accuracy when removed from the crankcase, but not inside the combustion chamber, where at least two layers could be removed. These are not removed in any of the suggested final models however, since removing them did not have much of an impact on the simulation time.

The adaptive time step did not have a major impact on the accuracy of the results, but saved a significant amount of time. This modification in the setup could be used for most design modifications, since the time step will be automatically adjusted if the velocities of the flow are affected. For higher limits than 0.75 CAD, the mass conservation error could become a problem since it can be seen to increase as the limit on the timestep increases. The mass conservation when using the adaptive timestep is computed by integrating the mass flows in Python instead of doing it in Star-CCM+ directly as the other setups. This computation is affected by the difference in step size over the cycle, which gives different resolutions of the flow rates. The flow into the combustion chamber has a higher resolution than the mass flows through the Af- and Ah-ports, due to the ports being open during different parts of the cycle, which affects the values of the integrals. If the overset meshes are removed and another method is used to handle the moving parts instead, the need to monitor the mass conservation disappears.

All simulations, including the ones for the time data, were run on 256 cores that are part of a big cluster. This makes it difficult to ensure the same nodes are used for each simulation. Due to this, the simulation time could be affected slightly depending on which nodes that are used.

The simulation with a single gas formulation looks promising in regard to timesavings. There are still some small issues that need to be resolved before a definitive conclusion about the accuracy of the model can be drawn, since the temperatures and pressures inside the combustion chamber are far from the reference values at the moment. The next step of improving the simulation could be to look into the specific heat and the density of the gas and connect them to the passive scalar. At the moment, the density differs compared to the reference, since the gas composition varies as the combustion process progresses. Since the density changes depending on the gas composition, and is present in the calculations leading to the HRR, this will influence the temperature in the combustion chamber. The specific heat is also dependent on the gas composition, and the polynomial used might not be representative. One possible solution to this could be to use two passive scalars to track the fluid inside the engine, one for the incoming fluid and one for the residual gases from the combustion. Then the properties could be set separately for the fresh fuel mixture and for the residual gases. Since this change does not directly connect to the other modifications, the timesaving it provides could be scalable into a combined model and therefore save about 38% on the model it is applied to. This makes it relevant for future development. This setup would also be useful for all kinds of design changes since the level of information is not impaired when the pressures and total mass flows are of interest.

The final setup is the combination of the replaced rod, the mesh with a size of 120% of the original in the core of the engine, excluding the combustion chamber, and 300% of the original in the inlet and outlet. It also utilizes an adaptive time step with a maximum time step of 0.6 CAD. In total, it takes 68.3% less time to run than the original model while still maintaining good results.

7

Declaration of AI Usage

During the duration of this thesis, AI in the form of Copilot has mostly been used to help troubleshoot the simulation software. It has also been used to find useful functionalities in the LaTeX editor and Python functions well-suited for our needs. Finally, Grammarly and the grammatical assistant integrated in Overleaf have been used to catch grammatical errors in the report.

Bibliography

[1] Husqvarna University, “Animation fuel injection,” unpublished.

[2] L. Klepáč and D. Rozehnal, “The analysis of exhaust emissions at different placemens of low pressure fuel injectors in two stroke engine,” in *2019 International Conference on Military Technologies (ICMT)*, 2019, pp. 1–5. DOI: 10.1109/MILTECHS.2019.8870124. Accessed: Jan. 28, 2026.

[3] J. Ghojel, “Review of the development and applications of the wiebe function: A tribute to the contribution of ivan wiebe to engine research,” *International Journal of Engine Research*, vol. 11, p. 297, May 2010. DOI: 10.1243/14680874JER06510. Accessed: Jan. 20, 2026. [Online]. Available: https://www.researchgate.net/publication/235973540_Review_of_the_development_and_applications_of_the_Wiebe_function_A_tribute_to_the_contribution_of_Ivan_Wiebe_to_engine_research.

[4] A. Ferrari and P. Pizzo, “1.3 the working principle of modern si engines,” in *Injection Technologies and Mixture Formation Strategies for Spark-Ignition and Dual-Fuel Engines*. SAE International, 2022, ISBN: 978-1-4686-0311-8. Accessed: Feb. 20, 2026. [Online]. Available: https://app.knovel.com/kn/resources/kt0133HPT1/kpITMFSSI2/pdf.

[5] M. Bergman, R. Gustafsson, and B. Jonsson, “71 scavenging system layout of a 25 cc two-stroke engine intended for stratified scavenging,” SAE International, SAE Technical Paper 2002-32-1840, 2002. DOI: 10.4271/2002-32-1840. Accessed: Jan. 27, 2026. [Online]. Available: https://doi.org/10.4271/2002-32-1840.

[6] M. Jönsson, “Stratified scavenging computations in two-stroke engines using openfoam,” Master’s Thesis, Department of Applied Mechanics, Division of Fluid Dynamics, Gothenburg, Sweden, 2010. Accessed: Jan. 27, 2026. [Online]. Available: https://publications.lib.chalmers.se/records/fulltext/122640.pdf.

[7] J. G. Speight, “Chapter 10 - combustion of hydrocarbons,” in *Handbook of Industrial Hydrocarbon Processes*, J. G. Speight, Ed., Boston: Gulf Professional Publishing, 2011, pp. 355–393, ISBN: 978-0-7506-8632-7. DOI: https://doi.org/10.1016/B978-0-7506-8632-7.10010-6. Accessed: Feb. 17, 2026. [Online]. Available: https://www.sciencedirect.com/science/article/pii/B9780750686327100106.

[8] R. van Basshuysen and F. Schäfer, “22.1 fuels,” in *Internal Combustion Engine Handbook - Basics, Components, Systems, and Perspectives*. SAE Interna-

tional, 2004, ISBN: 978-0-7680-1139-5. Accessed: Mar. 20, 2026. [Online]. Available: https://app.knovel.com/kn/resources/kt0086HHK3/kpICEHBCS1/pdf.

[9] G. P. Blair, *The Basic Design of Two-Stroke Engines*. SAE International, Jan. 1990, ISBN: 978-0-7680-2306-0. DOI: https://doi.org/10.4271/R-104. Accessed: Feb. 16, 2026. [Online]. Available: https://doi.org/10.4271/R-104.

[10] R. van Basshuysen and F. Schäfer, "3.1 piston displacement and bore-to-stroke ratio," in *Internal Combustion Engine Handbook - Basics, Components, Systems, and Perspectives*. SAE International, 2004, ISBN: 978-0-7680-1139-5. Accessed: Feb. 19, 2026. [Online]. Available: https://app.knovel.com/kn/resources/kt0086GVW1/kpICEHBCS1/pdf.

[11] F. Lindström, Elmqvist, G. Kalghatgi, and A. H-E, "An empirical si combustion model using laminar burning velocity correlations," vol. 144, May 2005. DOI: 10.4271/2005-01-2106. Accessed: Jan. 20, 2026. [Online]. Available: https://www.researchgate.net/publication/268800350_An_Empirical_SI_Combustion_Model_Using_Laminar_Burning_Velocity_Correlations.

[12] A. J. Torregrosa, A. Broatch, P. Olmeda, and S. Aceros, "Numerical estimation of wiebe function parameters using artificial neural networks in si engine," in *SAE WCX Digital Summit*, SAE International, Apr. 2021. DOI: https://doi.org/10.4271/2021-01-0379. Accessed: Mar. 20, 2026. [Online]. Available: https://doi.org/10.4271/2021-01-0379.

[13] S. Szwaja, A. Piotrowski, M. Szwaja, and D. Musiał, "Thermodynamic analysis of the combustion process in hydrogen-fueled engines with egr," *Energies*, vol. 17, p. 2833, Jun. 2024. DOI: 10.3390/en17122833. Accessed: Mar. 20, 2026.

[14] V. Giglio and A. di Gaeta, "Novel regression models for wiebe parameters aimed at 0d combustion simulation in spark ignition engines," *Energy*, vol. 210, p. 118 442, 2020, ISSN: 0360-5442. DOI: https://doi.org/10.1016/j.energy.2020.118442. Accessed: Mar. 19, 2026. [Online]. Available: https://www.sciencedirect.com/science/article/pii/S0360544220315504.

[15] H. K. Versteeg and W. Malalasekera, *An introduction to computational fluid dynamics: the finite volume method*, 2nd ed. Essex, England: Pearson education, 2007. Accessed: Feb. 24, 2026. [Online]. Available: https://www.flowthermolab.com/wp-content/uploads/2021/11/Versteeg_Malalasekera_2ed.pdf.

[16] H. H. Hu, "Chapter 10 - computational fluid dynamics," in *Fluid Mechanics (Fifth Edition)*, P. K. Kundu, I. M. Cohen, and D. R. Dowling, Eds., Fifth Edition, Boston: Academic Press, 2012, pp. 421–472, ISBN: 978-0-12-382100-3. DOI: https://doi.org/10.1016/B978-0-12-382100-3.10010-1. Accessed: Jan. 28, 2026. [Online]. Available: https://www.sciencedirect.com/science/article/pii/B9780123821003100101.

[17] Vijayashree and V. Ganesan, "Application of cfd for analysis and design of ic engines," in *Advances in Internal Combustion Engine Research*, D. K. Srivastava, A. K. Agarwal, A. Datta, and R. K. Maurya, Eds. Singapore: Springer Singapore, 2018, pp. 251–306, ISBN: 978-981-10-7575-9. DOI: 10.1007/978-

981-10-7575-9_13. Accessed: Feb. 27, 2026. [Online]. Available: https://doi.org/10.1007/978-981-10-7575-9_13.

[18] X. Wang and H. Zhao, "A high-efficiency two-stroke engine concept: The boosted uniflow scavenged direct-injection gasoline (busdig) engine with air hybrid operation," *Engineering*, vol. 5, no. 3, pp. 535–547, 2019, ISSN: 2095-8099. DOI: https://doi.org/10.1016/j.eng.2019.03.008. Accessed: Mar. 23, 2026. [Online]. Available: https://www.sciencedirect.com/science/article/pii/S209580991830715X.

[19] H. Nilsson, *MTF073 Computational Fluid Dynamics, Ch_2 Lecture notes*. Nov. 1, 2024.

[20] B. Mohammadian, N. Namdari, A. H. Abou Yassine, J. Heil, R. Rizvi, and H. Sojoudi, "Interfacial phenomena in snow from its formation to accumulation and shedding," *Advances in Colloid and Interface Science*, vol. 294, p. 102 480, 2021, ISSN: 0001-8686. DOI: https://doi.org/10.1016/j.cis.2021.102480. Accessed: May 29, 2026. [Online]. Available: https://www.sciencedirect.com/science/article/pii/S0001868621001214.

[21] M. Gong and Y. Shen, "Study on heat flow decay in vertical jet of aircraft deicing fluid based on phase field and realizable k- turbulence model," *Thermal Science and Engineering Progress*, vol. 60, p. 103 446, 2025, ISSN: 2451-9049. DOI: https://doi.org/10.1016/j.tsep.2025.103446. Accessed: Apr. 22, 2026. [Online]. Available: https://www.sciencedirect.com/science/article/pii/S2451904925002367.

[22] L. Davidsson, *Fluid mechanics, turbulent flow and turbulence modeling*. 2026. Accessed: Apr. 23, 2026. [Online]. Available: https://www.cfd-sweden.se/lada/postscript_files/solids-and-fluids_turbulent-flow_turbulence-modelling.pdf.

[23] R. Raesi and E. A. Toorman, "Development and assessment of a new wall-free low-reynolds-number k– turbulence model," *International Journal of Heat and Fluid Flow*, vol. 120, p. 110 382, 2026, ISSN: 0142-727X. DOI: https://doi.org/10.1016/j.ijheatfluidflow.2026.110382. Accessed: Apr. 23, 2026. [Online]. Available: https://www.sciencedirect.com/science/article/pii/S0142727X26001487.

[24] R. Shaheed, A. Mohammadian, and H. K. Gildeh, "A comparison of standard k– and realizable k– turbulence models in curved and confluent channels," *Environmental Fluid Mechanics*, vol. 19, pp. 543–568, 2 2019, ISSN: 1573-1510. DOI: 10.1007/s10652-018-9637-1. Accessed: Apr. 23, 2026. [Online]. Available: https://doi.org/10.1007/s10652-018-9637-1.

[25] T.-H. Shih, W. Liou, A. Shabbir, Z. Yang, and J. Zhu. "A new k-e eddy viscosity model for high reynolds number turbulent flows-model development and validation," Accessed: Feb. 16, 2026. [Online]. Available: https://ntrs.nasa.gov/citations/19950005029.

[26] SiemensDigital Industries Software, *Simcenter StarCCM+ User Guide*, version 2502, Siemens, Munich, Germany, 2025.

[27] F. M White, *Fluid Mechanics Ninth Edition*, 6th ed. New York (NY), USA: McGraw Hill, 2008, ISBN: 9780071286459.

[28] H. Patel and M. Anto, "Oil splash simulation in final drive with overset mesh," Jan. 2019. DOI: 10.4271/2019-26-0274. Accessed: Jan. 27, 2026. [Online]. Available: https://saemobilus.sae.org/papers/oil-splash-simulation-final-drive-overset-mesh-2019-26-0274#view.

[29] S. Falk. "Introductory guide to overset simulations," Accessed: Feb. 13, 2026. [Online]. Available: https://community.sw.siemens.com/s/article/Introductory-Guide-to-Overset-Simulations.

[30] D. D. Chandar, "On overset interpolation strategies and conservation on unstructured grids in openfoam," *Computer Physics Communications*, vol. 239, pp. 72–83, 2019, ISSN: 0010-4655. DOI: https://doi.org/10.1016/j.cpc.2019.01.009. Accessed: Feb. 20, 2026. [Online]. Available: https://www.sciencedirect.com/science/article/pii/S0010465519300153.

[31] M. Schmitz, M. Biermann, A. Hörbe Emanuelsson, and F. Normann, *Formel- och tabellsamling: Termodynamik med Energiteknik*, Swedish. Chalmers Tekniska Högskola, Dec. 21, 2022.

[32] S. Makridakis, "Accuracy measures: Theoretical and practical concerns," *International Journal of Forecasting*, vol. 9, no. 4, pp. 527–529, 1993, ISSN: 0169-2070. DOI: https://doi.org/10.1016/0169-2070(93)90079-3. Accessed: Mar. 11, 2026. [Online]. Available: https://www.sciencedirect.com/science/article/pii/0169207093900793.

[33] J. Basharat and A. Naiem, "Comparative analysis of diffuse solar radiation models based on sky-clearness index and sunshine period for humid-subtropical climatic region of india: A case study," *Renewable and Sustainable Energy Reviews*, vol. 78, pp. 329–355, 2017, ISSN: 1364-0321. DOI: https://doi.org/10.1016/j.rser.2017.04.073. Accessed: May 5, 2026. [Online]. Available: https://www.sciencedirect.com/science/article/pii/S136403211730583X.

A

Pressure and Mass Flow Plots With a Lower Cutoff

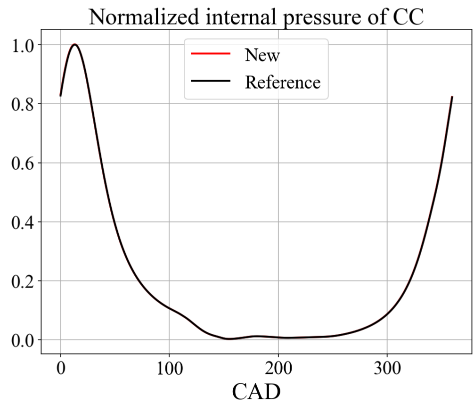

Figure A.1: Internal pressure inside the combustion chamber for the adaptive timestep with a maximum of 0.5 CAD and a cutoff of 0.5%.

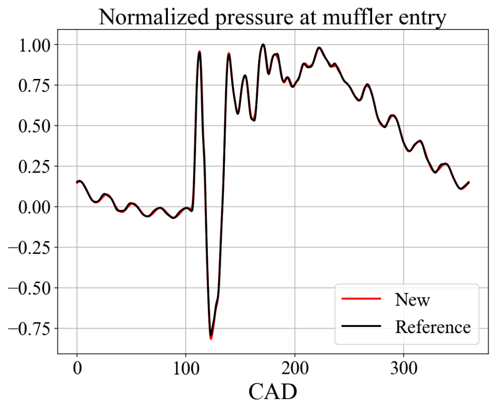

Figure A.2: Surface-averaged pressure at the inlet of the muffler for the adaptive timestep with a maximum of 0.5 CAD and a cutoff of 0.5%.

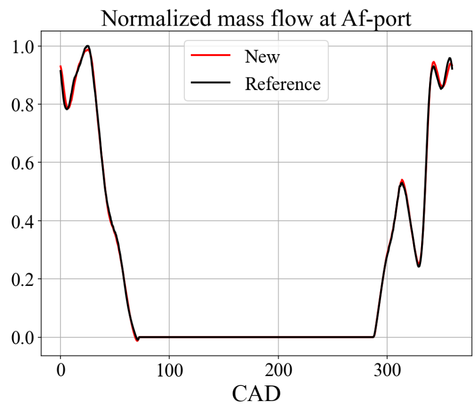

Figure A.3: Mass flow through the Af-port for the adaptive timestep with a maximum of 0.5 CAD and a cutoff of 0.5%.

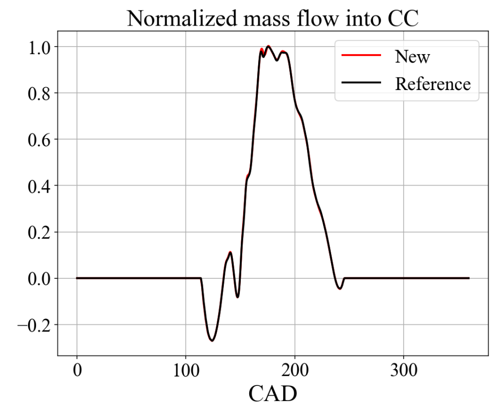

Figure A.4: Mass flow into the combustion chamber for the adaptive timestep with a maximum of 0.5 CAD and a cut-off of 0.5%.

B

Extra Plots From the Final Setup

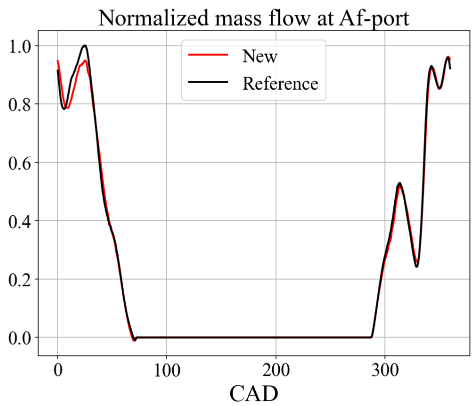

Figure B.1: Scaled mass flow through the Af-port for the final setup.

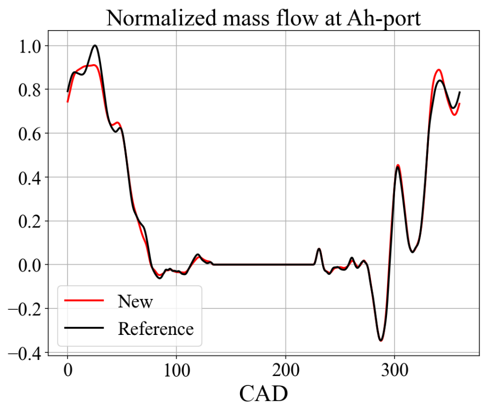

Figure B.2: Scaled mass flow through the Ah-port for the final setup.

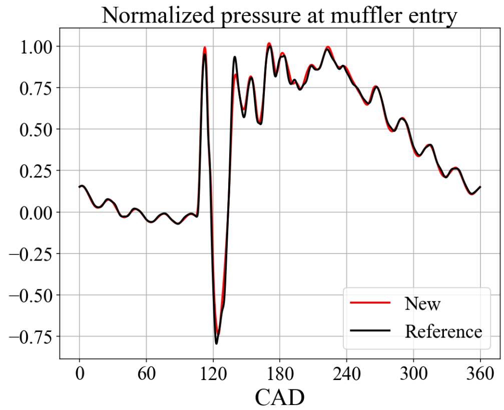

Figure B.3: Scaled pressure at the muffler inlet for the final setup.

DEPARTMENT OF MECHANICS AND MARITIME SCIENCES
CHALMERS UNIVERSITY OF TECHNOLOGY
Gothenburg, Sweden 2026
www.chalmers.se

CHALMERS
UNIVERSITY OF TECHNOLOGY